J. Fluid Mech. (2001), *vol.* 443, *pp.* 197–229. Printed in the United Kingdom

Free vibrations of two side-by-side cylinders in a cross-flow

By Y. ZHOU[1]†, Z. J. WANG[1], R. M. C. SO[1], S. J. XU[1] AND W. JIN[2]

[1]Department of Mechanical Engineering, The Hong Kong Polytechnic University, Hung Hom, Kowloon, Hong Kong

[2]Department of Electrical Engineering, The Hong Kong Polytechnic University, Hung Hom, Kowloon, Hong Kong

(Received 4 April 2000 and in revised form 27 March 2001)

Free vibrations of two side-by-side cylinders with fixed support (no rotation and displacement) at both ends placed in a cross-flow were experimentally investigated. Two fibre-optic Bragg grating sensors were used to measure the dynamic strain, while a hot wire and flow visualization were employed to examine the flow field around the cylinders. Three T/d ratios, 3.00, 1.70 and 1.13, were investigated, where T is the centre-to-centre cylinder spacing and d is the diameter; they give rise to three different flow regimes. The investigation throws new light on the shed vortices and their evolution. A new interpretation is proposed for the two different dominant frequencies, which are associated with the narrow and the wide wake when the gap between the cylinders is between 1.5 and 2.0 as reported in the literature. The structural vibration behaviour is closely linked to the flow characteristics. At $T/d = 3.00$, the cross-flow root-mean-square strain distribution shows a very prominent peak at the reduced velocity $U_r \approx 26$ when the vortex shedding frequency f_s, coincides with the third-mode natural frequency of the combined fluid–cylinder system. When $T/d < 3.00$, this peak is not evident and the vibration is suppressed because of the weakening strength of the vortices. The characteristics of the system modal damping ratios, including both structural and fluid damping, and natural frequencies are also investigated. It is found that both parameters depend on T/d. Furthermore, they vary slowly with U_r, except near resonance where a sharp variation occurs. The sharp variation in the natural frequencies of the combined system is dictated by the vortex shedding frequency, in contrast with the lock-in phenomenon, where the forced vibration of a structure modifies the vortex shedding frequency. This behaviour of the system natural frequencies persists even in the case of the single cylinder and does not seem to depend on the interference between cylinders. A linear analysis of an isolated cylinder in a cross-flow has been carried out. The linear model prediction is qualitatively consistent with the experimental observation of the system damping ratios and natural frequencies, thus providing valuable insight into the physics of fluid–structure interactions.

1. Introduction

When a two-dimensional bluff body/cylinder is subject to a cross-flow, vortex shedding from the structure creates fluid excitation forces which, in turn, cause the

† Author to whom correspondence should be addressed: e-mail mmyzhou@polyu.edu.hk

structure to vibrate. The resultant structural motions influence the flow field, giving rise to fluid–structure coupling and modifying the frequency and magnitude of the induced forces. The coupling is in general a highly nonlinear function of the structural motion and flow velocity and is not well understood. Since flow-induced vibrations have significant impact on the fatigue life of structures and could have disastrous consequences, interest in understanding the associated physics and predicting the structural motions is rapidly growing (Blevins 1994; Ziada & Staubli 2000).

Flow-induced vibration is governed by a number of major parameters. Among these are the reduced velocity, U_r, the damping ratio and the mass ratio (Chen 1987). Each of these parameters plays a different role in the dynamic response of the cylinder. The damping ratio is the ratio of the energy dissipated by the system to the total system energy. The mass ratio, which is the ratio of the cylinder mass to the displaced fluid mass, provides a measure of the relative importance of the different fluid force components. The reduced velocity U_r, defined by $U_\infty/f_0^{(1)}d$, where U_∞ is the free-stream velocity, d is the cylinder diameter and $f_0^{(1)}$ is the first-mode natural frequency of a stationary cylinder, is linked to the ratio of the vortex shedding frequency f_s to the structural natural frequency. Here, the term structural natural frequency is used loosely to mean the structural natural frequency of any one of the vibration modes, but is usually taken to imply the first mode. The natural frequency is the vibration frequency with which a structure or system, after an initial disturbance, oscillates without external forces. In a vortex-induced free vibration problem, f_s is responsible for the creation of the unsteady forces. Therefore, the interplay between the two frequencies determines the resultant behaviour of the cylinder dynamics and the wake structure. This is especially true when resonance (or synchronization) occurs, which can be loosely defined as the situation where f_s is approximately equal to the structural natural frequency. Strictly speaking, resonance occurs when the natural frequency of the combined fluid–structure system is equal to f_s. However, the natural frequency of the system and, to a certain extent, f_s are not known *a priori*. Therefore, the fluid–structure interaction problem is very complicated and its behaviour at or near resonance is of great interest to engineers.

The free vibration problem is further complicated by the presence of an identical neighbouring cylinder, such as in the case of two side-by-side cylinders. Here, besides the parameters mentioned above, the problem is also governed by the ratio of the centre-to-centre cylinder spacing T to diameter d. Varying this ratio could lead to the formation of a single or multiple wakes (Landweber 1942; Spivac 1946; Ishigai *et al.* 1972; Bearman & Wadcock 1973; Zdravkovich 1985; Zhou *et al.* 2000*a*) and this, in turn, could affect the dynamic response and the resonance behaviour of the cylinders. Furthermore, the nonlinear interplay between the simultaneous vibrations of the two cylinders and the fluid as a result of flow-induced forces is a far more complicated process than the fluid–cylinder interaction in the single cylinder case.

Interference between circular cylinders placed side-by-side in a cross-flow has been investigated extensively (Zdravkovich 1977) because of its inherent importance and practical significance in many branches of engineering. The interference drag measurements of two side-by-side cylinders facing a uniform flow can be traced back to Biermann & Herrnstein (1933). Zdravkovich & Pridden (1977) measured the lift and drag coefficients and noted that the sum of the low and high drag generated by the two cylinders was always less than twice the drag of a single cylinder. Using a photographic method, Landweber (1942) observed a single vortex street for $T/d \leqslant 1.5$ and two distinct vortex streets for $T/d > 2$. Spivac (1946) measured two different frequencies in the two-cylinder wake for $T/d < 2$ but a single frequency for $T/d > 2$.

In the latter case, the frequency was further found to be the same as that measured in the single cylinder wake. A Schlieren optical method was used by Ishigai *et al.* (1972) to visualize the flow behind two side-by-side cylinders. They observed a remarkably symmetric vortex formation and shedding for $T/d = 2.5$ and 3.0, but a biased gap flow for $1.5 < T/d < 2.0$. The biased flow was bi-stable and intermittently changed over from one side to another, forming two asymmetric vortex streets of different frequencies. Bearman & Wadcock (1973) have made a similar observation in their experiments. Based on flow visualization at a low Re ($\leqslant 200$), Williamson (1985) suggested that the two different frequencies, observed in the asymmetric flow regime ($1.5 \leqslant T/d \leqslant 2.0$), were due to the existence of harmonic vortex-shedding modes. On the other hand, the measurements of Kim & Durbin (1988) at $Re = 3300$ did not support this conjecture. Therefore, the mechanism for the two distinct frequencies in the asymmetric flow regime has yet to be properly understood.

Previous studies were mostly concerned with the behaviour of the wake flow and the flow-induced vibrations on rigid cylinders. Even in the free vibration case, the cylinders, flexibly mounted at both ends, were relatively rigid. Here, a rigid cylinder is defined as one having infinite structural stiffness. The dynamic characteristics of an elastic cylinder, defined as one with finite structural stiffness, fix-supported at both ends (no deflection), can be quite different from a rigid one. For example, there is only one natural frequency for a rigid cylinder system but more than one associated with an elastic cylinder system (Zhou *et al.* 1999; So, Zhou & Liu 2000). There have been relatively few studies on two side-by-side elastic cylinders in a cross-flow. Consequently, many issues remain to be resolved. For example, how is the free vibration of an elastic cylinder in a cross-flow affected by the presence of a neighbouring cylinder? In a forced vibration situation, the imposed vibration modifies the vortex shedding frequency. However, in the free vibration case, the vortex shedding generates the excitation forces. Could the vortex shedding modify the natural frequencies of the fluid–cylinder system? Are these frequencies dependent on T/d and U_r?

Damping is another important issue. It models the energy dissipation of the system during vibration and plays an important role in the stability of a structure and its vibration amplitude. Knowledge of damping is essential if the dynamic behaviour of the structures in a cross-flow is to be understood thoroughly. Damping arises from the fluid surrounding the structure as well as from the structure itself. While structural damping is related to the properties of the structure alone, fluid damping originates from viscous dissipation and fluid drag. In other words, fluid damping is the result of viscous shearing of the fluid at the surface of the structure and the behaviour of flow separation. Therefore, it is motion dependent and is much more difficult to estimate. Using an auto-regressive moving average (ARMA) analysis technique, Zhou, So & Mignolet (2000*b*) and So *et al.* (2001) deduced the effective and fluid damping ratios from the calculated lift and displacement signals of a single cylinder in a cross-flow over a range of Re. In these studies, the cylinder motion was modelled by a two-degree-of-freedom system. Later, Wang, So & Liu (2000) used the same technique to analyse similar signals derived by employing the Euler–Bernoulli beam theory to model the free vibration of a single cylinder. All these studies yield reasonable results compared to measured fluid damping ratios. In particular, Wang *et al.* (2000) were able to deduce the fluid damping ratios for the first and third mode of vibration. However, the issue of how interference between cylinders affects the damping ratios has yet to be addressed. It is not clear whether damping behaviour is, if at all, related to the system natural frequencies.

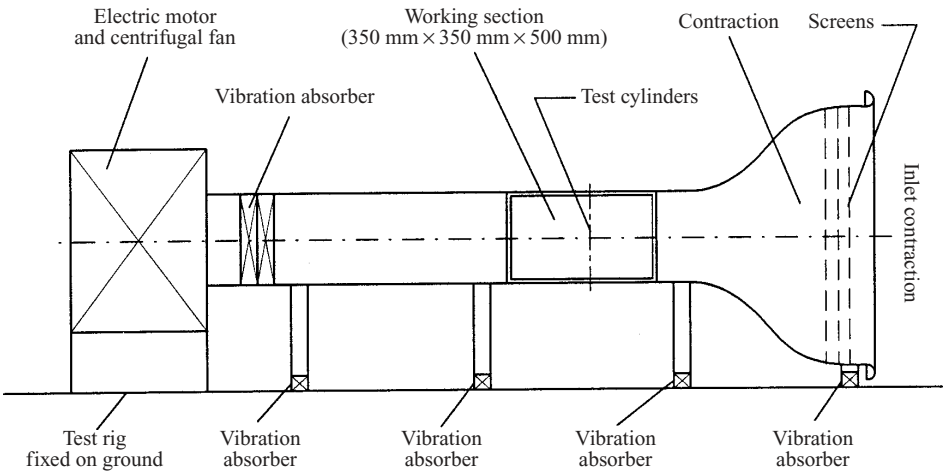

FIGURE 1. Schematic diagram of the test wind tunnel.

The present work aims to investigate experimentally the free vibration of two side-by-side cylinders placed in a cross-flow and the associated nonlinear fluid–cylinder interactions. The first objective is to improve the understanding of the flow structure around the cylinders, including the mean pressure distribution, the induced lift and drag, and the vortex formation and its evolution at different T/d ratios. In particular, the two distinct frequencies in the asymmetric flow regime are examined based on flow visualization and hot-wire signals. The second objective is to study fluid–structure interactions. The free vibration of the two cylinders due to flow excitation is characterized in detail. The dependence on T/d and U_r of the natural frequency of the combined fluid–structure system is investigated thoroughly, in particular at and near resonance. The effective and fluid damping ratios are evaluated from the measured strain signals using an ARMA technique (Mignolet & Red-Horse 1994). The observations from measurements are further discussed in conjunction with a linear analysis of the fluid–cylinder system in order to gain a better understanding of the physics associated with fluid–structure interactions.

2. Experimental details

2.1. *Experimental setup*

Experiments were carried out in a suction-type wind tunnel with a 0.35 m × 0.35 m square cross-section that is 0.5 m long (figure 1). The wind speed of the working section can be adjusted from 1.5 to 28 m s^{-1}. The streamwise velocity is uniform to within 0.05% and the free-stream turbulence intensity is 0.2%. In order to minimize tunnel vibrations, the working section is isolated from the motor and fan through vibration absorbers. More details of the tunnel are given in Zhou *et al.* (1999) and So *et al.* (2000).

Two identical acrylic tubes with a diameter of $d \approx 0.006$ m were mounted vertically in a side-by-side arrangement and placed symmetrically to the mid-plane of the working section at 0.20 m downstream of the exit plane of the tunnel contraction (figures 1 and 2). The coordinate system is attached to Cylinder 1 with y equal to zero at the centre of this cylinder (figure 2), and the other is labelled Cylinder 2. The two cylinders were built into the walls of the working section, with fix-supported

				$f_0^{(1)}$(Hz)					
				T/d (cross-flow direction)			T/d (inline direction)		
Cylinder	EI(N m^2)	M^*	$\zeta_0^{(1)}$	1.13	1.70	3.00	1.13	1.70	3.00
1	0.224	565	0.026	104.00	104.00	104.00	98.60	98.60	98.60
2	0.224	565	0.026	94.00	95.00	101.00	95.83	101.50	101.53

TABLE 1. Structural characteristic properties of the cylinders.

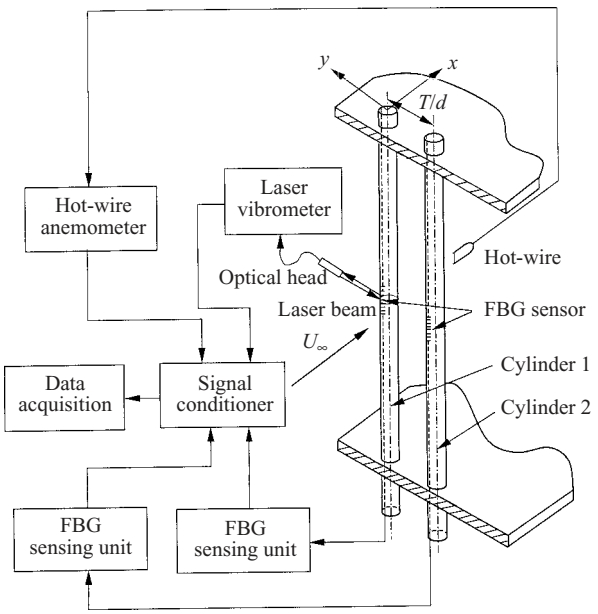

FIGURE 2. Experimental arrangement.

boundary conditions at both ends (no rotation and displacement). The structural characteristic properties of the cylinders are summarized in table 1. Here, E is the Young's modulus of the cylinder, I is the area moment of inertia, $\zeta_0^{(1)}$ is the first-mode structural damping ratio and M^* is the mass ratio defined by $M/\rho d^2$, where ρ is the fluid density and M is the cylinder mass, and $f_0^{(1)}$ is the first-mode structural natural frequency. The blockage due to the installation of the cylinders was about 3.4%. The Reynolds number, $Re = U_\infty d/\nu$, where ν is the fluid kinematic viscosity, varied from 800 to 10 000. This gives rise to a U_r range of 3–43. In the present Re range, the blockage effect on the mean drag is insignificant. Three transverse spacing ratios were investigated, $T/d = 1.13$, 1.70 and 3.00. Great care was taken to maintain these ratios along the cylinder span. Furthermore, they were chosen because the flow regimes thus resulting were representative of the different proximity effects for two side-by-side cylinders (Zdravkovich 1985).

2.2. *Mean drag and lift measurements*

The experimental arrangement is shown schematically in figures 1 and 2. Each of the cylinders was instrumented with a single wall-pressure tap at the mid-span position. A pressure transducer was connected to the tab to measure the wall static pressure. The cylinder was rotated in intervals of 5° to give the angular distribution of wall static pressure around the cylinder surface and the mean lift and drag on the cylinder were evaluated by integrating the wall static pressure around the cylinder. Measurements of the mean lift and drag were carried out on a single cylinder and on the two side-by-side cylinders at the same *Re*, thus providing a baseline for the evaluation of the interference effects.

2.3. *Fluctuating velocity measurements*

The streamwise fluctuating velocity u was measured by positioning a single hot wire at $x/d = 2$ and $y/d = 1.5$, where x is the streamwise distance measured from the centre of Cylinder 1 (figure 2). The hot wire was operated at an overheat ratio of 1.8 with a constant temperature anemometer (DISA Type 55M10).

2.4. *Dynamic strain measurements*

Zhou *et al.* (1999) and Jin *et al.* (2000) used a fibre-optic Bragg grating (FBG) sensor, built in-house, to measure the dynamic strain due to lift on a cylinder in a cross-flow. The strain thus measured was compared with the transverse displacements obtained from a laser vibrometer. They found that the spectra deduced from the two signals were in excellent agreement with each other in terms of their salient features, such as the vortex shedding frequency and the natural frequency of the fluid–cylinder system, and the two signals showed a complete coherence at these frequencies. They further found that, for small displacements, the root-mean-square (r.m.s.) values of the strain and displacement signals were linearly correlated. A linear correlation is also expected between strain and displacement due to the fluctuating drag and in the presence of another cylinder.

Two FBG sensors were used to simultaneously measure the dynamic strains of the two cylinders along the x- or y-direction. For measurement along the y-direction, an optical silica fibre of diameter 125 μm built with an FBG sensor was buried in a groove along the span of each cylinder at 90° from the leading stagnation line and flushed with the surface using nail polish. The FBG sensor was located at mid-span of the cylinder. Since the sensor grating has a finite length of about 10 mm, the measurement represents the average strain over this length. The strain thus measured is designated as ϵ_y. In principle, ϵ_y is independent of the streamwise vibration of the structure. If the cylinder is rotated clockwise (or anti-clockwise) by 90°, the FBG sensor will be located at the rear stagnation line (or the leading stagnation line). At this location, it measures the strain ϵ_x, due to the drag, which should not depend on the cross-flow vibration of the cylinder. A major source of error comes from the nonlinearity effect when calibrating the relation between the output voltage and strain (Zhou *et al.* 1999; Jin *et al.* 2000). The experimental uncertainty in strain measurements is estimated to be $\pm 8\%$.

In view of the fact that mounting and remounting a cylinder might change the natural frequency of the structure, the mounting of Cylinder 1 was not changed during the entire experiment where the dynamic strain for either the cross-flow or inline direction was measured. Therefore, $f_0^{(1)}$ of Cylinder 1 was constant. Its value is 104 Hz for the cross-flow direction and 98.60 Hz for the inline direction (table 1). This arrangement is important if the interference effect on the natural frequencies

of the fluid–cylinder system is to be investigated with confidence. The adjustment of T/d was achieved by remounting Cylinder 2 only. Great care was taken to minimize the variation of $f_0^{(1)}$ associated with remounting. The $f_0^{(1)}$ values of Cylinder 2 in both cross-flow and inline directions are given in table 1. Measurements of the bending displacement Y and u in the wake of a single cylinder carried out by Zhou *et al.* (1999) indicated a negligible effect on flow separation around the cylinder and on Y due to the attachment of the optical fibre.

The signals u, ϵ_{y1} and ϵ_{y2} or u, ϵ_{x1} and ϵ_{x2}, where the subscripts 1 and 2 represent the cylinder number, were simultaneously measured. They were offset, amplified and digitized using a 12 bit A/D board and a personal computer at a sampling frequency of 6.0 kHz per channel. The record length was about 20 s. This record length was sufficiently long for the r.m.s. values $\epsilon_{x,rms}$ of ϵ_x and $\epsilon_{y,rms}$ of ϵ_y to reach their stationary state, with a variation smaller than 1.0%.

2.5. *Effect of tunnel vibrations*

It is important to minimize tunnel vibrations in the present investigation. As pointed out earlier, tunnel vibrations were mainly derived from the fan and motor. Great care has been taken to isolate the working section from the vibration sources through the use of vibration absorber (figure 1). This vibration isolation is not a sufficient remedy for the laser vibrometer measurement of displacement because the motion of the working section, which can be transmitted through the floor, also affects the measurements (Zhou *et al.* 1999). The FBG sensor, on the other hand, measures the cylinder deformation. Therefore, it is insensitive to any translational motion of the cylinder, which is associated with the working section vibration. Tunnel vibrations only indirectly affect the FBG sensor measurements through the inertia force. However, this is a secondary effect and is unlikely to have a significant impact on the measurements as demonstrated below.

The effect of tunnel vibrations could be estimated by calculating the variation in energy corresponding to the first-mode natural frequency, with and without tunnel vibrations. The power spectra $E_{\epsilon y}$ of ϵ_y from Cylinder 1 for $T/d = 1.13$, 1.70 and 3.00 at $U_r = 11.0$ is shown in figure 3. Here, $E_{\epsilon y}$ is normalized so that $\int_0^\infty E_{\epsilon y}(f)\,\mathrm{d}f = 1$. In figure 3(*a*), $E_{\epsilon y}$ calculated from the original strain signal is shown. The half-power-bandwidth (HPB) integral at the first-mode natural frequency of the fluid–structure system is 40.77%, 4.17% and 10.07% for $T/d = 1.13$, 1.70 and 3.00, respectively. The natural frequency of the working section was measured in the range of 20–30 Hz (Zhou *et al.* 1999). Therefore, the measured ϵ_y was high-pass filtered at 60 Hz to eliminate the noise associated with tunnel vibrations. The $E_{\epsilon y}$ calculated from the filtered signal is plotted in figure 3(*b*) and the HPB integral at the first-mode natural frequency is 41.68%, 5.06% and 11.19% for $T/d = 1.13$, 1.70 and 3.00, respectively. The maximum difference between the $E_{\epsilon y}$ calculated with and without filtering is about 1.1%, indicating a negligible tunnel vibration effect on the FBG sensor measurements.

2.6. *Flow visualization*

Flow visualization was carried out in a water tunnel with a 0.15 m × 0.15 m square working section 0.5 m long. The water tunnel is a recirculating single-reservoir system. From the reservoir, a centrifugal pump delivers water to the tunnel contraction. A honeycomb is used to remove any large-scale irregularities prior to the contraction. The flow speed is controlled by a regulator valve up to a maximum velocity of about 0.32 m s^{-1} in the working section. The working section is made up of four 20 mm thick

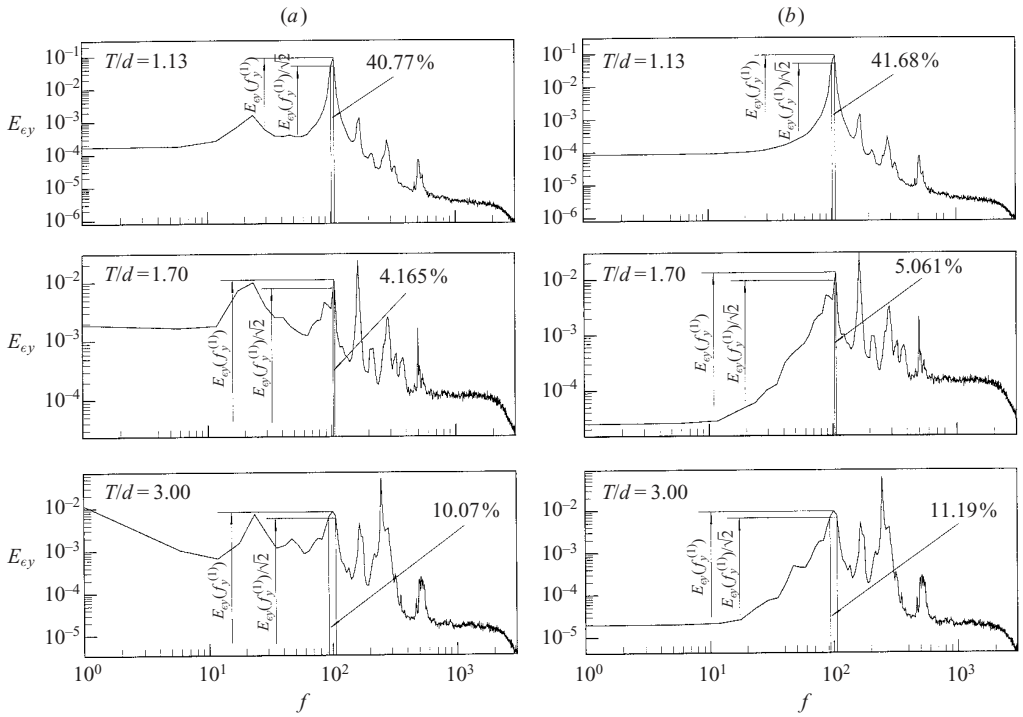

FIGURE 3. Power spectra $E_{\epsilon y}$ of ϵ_y: (*a*) calculated from the measured signal; (*b*) from the signal filtered with a high pass of 60 Hz. Cylinder 1; $U_r = 11.0$.

Perspex panels. Two side-by-side acrylic circular tubes with an identical diameter of 10 mm were horizontally mounted 0.20 m downstream of the exit plane of the tunnel contraction and placed symmetrically to the mid-plane of the working section. They spanned the full width of the tunnel. The resulting blockage was 13.3%. For the purpose of comparison with the FBG sensor measurements, the same transverse spacing ratios as those used in the wind tunnel were investigated, i.e. $T/d = 1.13$, 1.70 and 3.00. For each cylinder, dye (Rhodamine 6G 99% which has a faint red colour and will become metallic green when excited by laser) was introduced through injection pinholes located at the mid-span of the cylinder at 90°, clockwise and anti-clockwise, respectively, from the forward stagnation point. A thin laser sheet, which was generated by laser beam sweeping, provided illumination vertically at the mid-plane of the working section. A Spectra-Physics Stabilite 2017 Argon Ion laser with a maximum power output of 4 W was used to generate the laser beam and a digital video camera recorder (Sony DCR-PC100E), set perpendicular to the laser sheet, was used to record the dye-marked vortex streets. Investigations of flow visualization were carried out in the *Re* range of 120 to 1650 over $0 \leqslant x/d \leqslant 10$. At large *Re* and x/d, the dye diffused too rapidly to be an effective marker of vortices.

3. Fluid dynamics around cylinders

3.1. *Mean pressure, lift and drag*

The polar plots of pressure coefficient, $C_p = 2\Delta p/(\rho U_\infty^2)$, around the cylinder for a single as well as two side-by-side arrangements at $Re = 6000$ are shown in figure 4. Here, Δp is the mean pressure difference between the cylinder wall and a reference

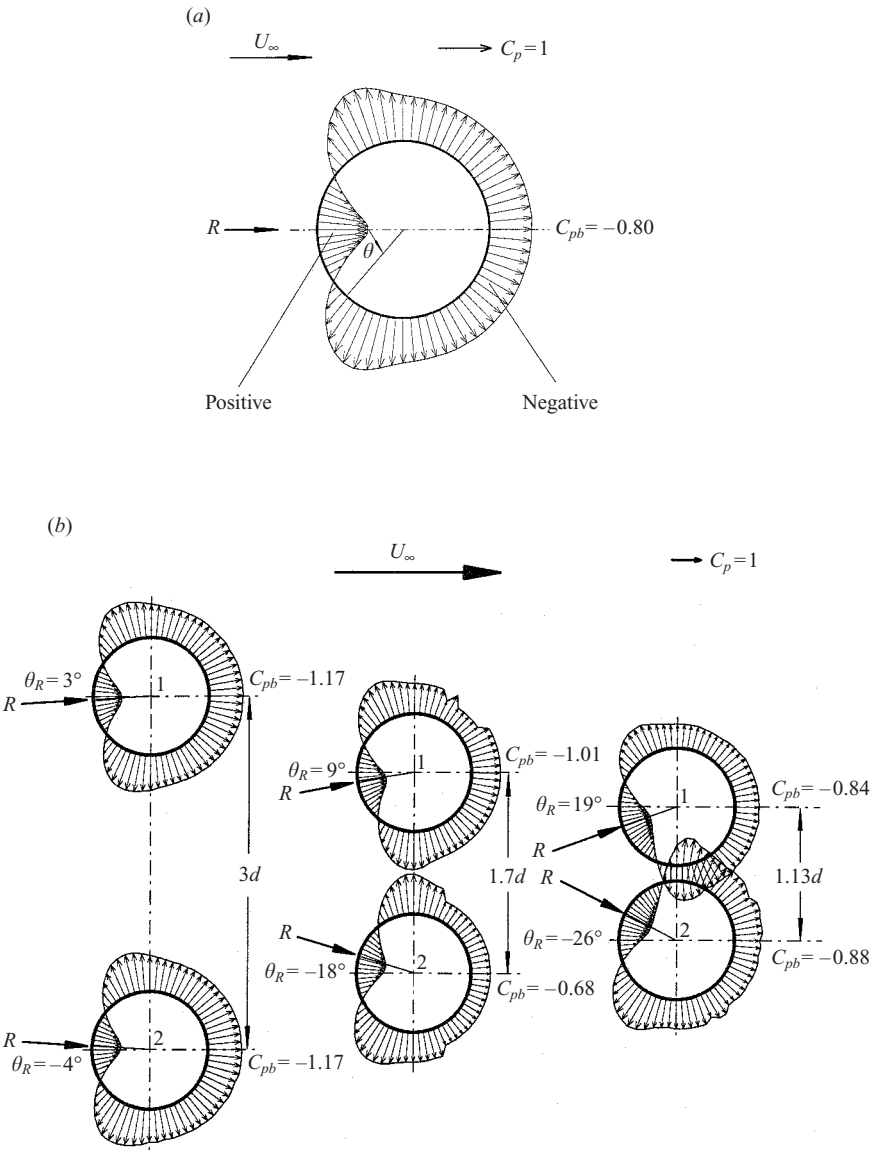

FIGURE 4. Polar plot of the circumferential distribution of pressure coefficient. (*a*) Single cylinder; (*b*) two cylinders at three different T/d values. $Re = 6000$.

point upstream. The resultant force R is calculated from $\sqrt{D^2 + L^2}$ and its direction is given by the angle $\theta_R = \tan^{-1}(L/D)$, where L and D are the mean lift and drag, respectively. Mean lift and drag of the two cylinders are calculated by integrating the pressure around the cylinders. The respective force coefficients are defined by $C_L = 2L/(\rho U_\infty^2 d)$ and $C_D = 2D/(\rho U_\infty^2 d)$. Their values thus deduced for $Re = 3500$, 6000 and 10 400 are shown in figures 5(*a*) and 5(*b*).

The pressure distributions of the two cylinders at $T/d = 3.0$ exhibit similarity to that for a single cylinder. But the resultant force on each cylinder deviates from the flow direction, probably as a result of flow retardation upstream of the gap between the cylinders, which could give rise to a higher pressure between the cylinders. The θ_R

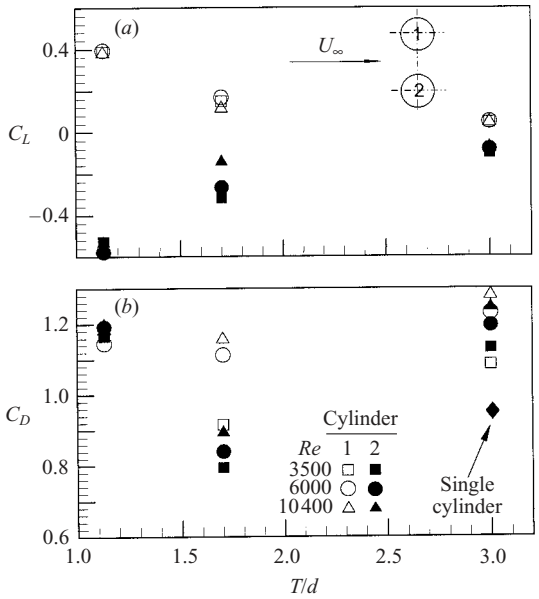

FIGURE 5. Dependence of (*a*) lift and (*b*) drag coefficients on the spacing ratio T/d.

is 3° for Cylinder 1 and −4° for Cylinder 2. The difference in magnitude is probably caused by experimental uncertainty, which is estimated to be about 2.5°. Therefore, the pressure distribution around one cylinder is essentially a mirror image of the other. For $T/d < 3.0$, the pressure distributions around the two cylinders are no longer mirror images of each other, as evidenced by the difference in θ_R and the base pressure coefficient C_{pb} ($\theta = 180°$) between the cylinders. However, in each case, R is directed approximately through the forward stagnation point, where the pressure is the maximum, and the cylinder centre. The observation is essentially the same as that reported in Bearman & Wadcock (1973).

C_L is positive for Cylinder 1 and negative for Cylinder 2 (figure 5*a*), showing a repulsive force between the cylinders. Since flow upstream of the gap between the cylinders is further retarded as T/d reduces, the pressure rises between $\theta \approx 0°$ and 90° for Cylinder 1 and between $\theta \approx 270°$ and 360° for Cylinder 2 (figure 4*b*). As a result, the repulsive force between the cylinders increases with decreasing T/d.

At $T/d = 3.0$, C_D is approximately the same for the two cylinders (figure 5*b*), ranging from 1.08 to 1.27 when Re varies from 3500 to 10 400, comparable to that, 0.93, of a single cylinder. At $T/d = 1.70$, the drag coefficients of the two cylinders become different. This can be inferred from the base pressure coefficient C_{pb} at $\theta = 180°$. The value is about −1.01 for Cylinder 1 (figure 4*b*). The lower value of C_{pb} gives rise to a higher C_D. On the other hand, C_{pb} of Cylinder 2 is about −0.68 (figure 4*b*), resulting in a lower C_D. It is well known that, for this T/d, narrow and wide wakes are formed behind two identical cylinders, respectively, and the gap flow deflects towards the narrow wake (Zdravkovich 1987). Bearman & Wadcock (1973) and Quadflieg (1977) observed that the narrow wake has a lower base pressure and a higher C_D, whereas the wide wake has a higher base pressure and a lower C_D. Thus, it may be inferred that Cylinders 1 and 2 are mostly associated with a narrow and a wide wake, respectively. At $T/d = 1.13$, C_{pb} shows an increase for both cylinders. However, C_p between 0° and 90° for Cylinder 1 and 270° and 360° for Cylinder 2

also increases significantly, due to more severe flow retardation upstream of the gap between the cylinders. Consequently, C_D is higher for both cylinders. There is still a difference in the measured C_D between the two cylinders, though less pronounced than that obtained at $T/d = 1.70$. At such a small T/d, a single vortex street is expected behind the cylinders (Landweber 1942). Photographs from laser-illuminated flow visualization shown in § 3.2 indicate a biased bleeding between the cylinders. The biased bleeding probably accounts for the difference in the C_p distribution between the cylinders (figure 4*b*), and hence unequal C_D for the two cylinders.

The mean of the low and high C_D values at $T/d = 3.00$ is 1.2, appreciably higher than that (0.93) of a single cylinder at $Re = 6000$. The difference cannot be attributed to the experimental uncertainty, which is estimated to be 2%. Further investigation is needed to understand this observation. For $T/d < 3.00$, this mean is generally less than that determined at $T/d = 3.00$, consistent with that reported in Zdravkovich & Pridden (1977). In the near wake of an isolated cylinder, about 50% of the shed circulation was cancelled as fluid bearing vorticity was drawn across the wake centreline into the growing vortex with opposite vorticity (Gerrard 1966; Cantwell & Coles 1983). One would expect that the interference between the narrow and wide wakes might cause additional cancellation of vorticity as well as absorb some flow energy, thus resulting in reduced vortex strength. This, in turn, causes a higher base pressure as exhibited in figure 4, hence a reduced total drag.

3.2. *Flow patterns*

The above interpretation is further verified by the observations from the flow visualization experiment. In this section, flow visualization results for the three cases, $T/d = 1.13$, 1.70 and 3.00, are examined with the aim to gain an understanding of the flow physics. The characteristics of the spectral characteristics are discussed later.

$T/d = 3.0$: Figure 6(*a*) shows typical photos in the laminar ($Re = 150$) and turbulent ($Re = 450$) flow regime, respectively, both exhibiting two anti-phase vortex streets. The pattern is consistent with that reported in the literature. Flow visualization conducted at $Re = 500$ by Bearman & Wadcock (1973) showed that two pairs of vortices, when shed from the two cylinders at $T/d = 3.00$, were in an anti-phase mode. In their experiments, Ishigai *et al.* (1972) observed a remarkably symmetric vortex formation and shedding for $T/d = 2.5$ and 3.0, but a biased gap flow when T/d was in the range, $1.25 < T/d < 2.0$. The present data suggest that the phenomenon is independent of Re in the range investigated.

The mechanism behind the symmetric vortex shedding behaviour is not clear. Weaver & Abd-Rabbo (1984) and Granger, Campistron & Lebret (1993) observed a symmetric vortex shedding resonance in a square array of tubes in a cross-flow. Weaver & Abd-Rabbo proposed that a symmetric-mode jet instability mechanism might have caused or at least triggered this phenomenon. Noting that during resonance the vibration amplitude was predominant in the streamwise direction, Granger *et al.* (1993) suggested that the inline cylinder motion caused a symmetric oscillation of separation points at the surface of the moving cylinder and could be responsible for the symmetric vortex shedding. This cannot explain the present symmetric vortex shedding at $T/d = 3.00$. It will be seen in the next section that the cross-flow vibration of the cylinders overwhelms the streamwise vibration when resonance occurs. The inline cylinder motion is unlikely to be, at least not solely, responsible for the present symmetric vortex shedding. When flow separation occurs, the flow outside the boundary layer is retarded (Prandtl 1935), implying a higher pressure. The pressure upstream of the gap between the cylinders is probably even higher than that close to

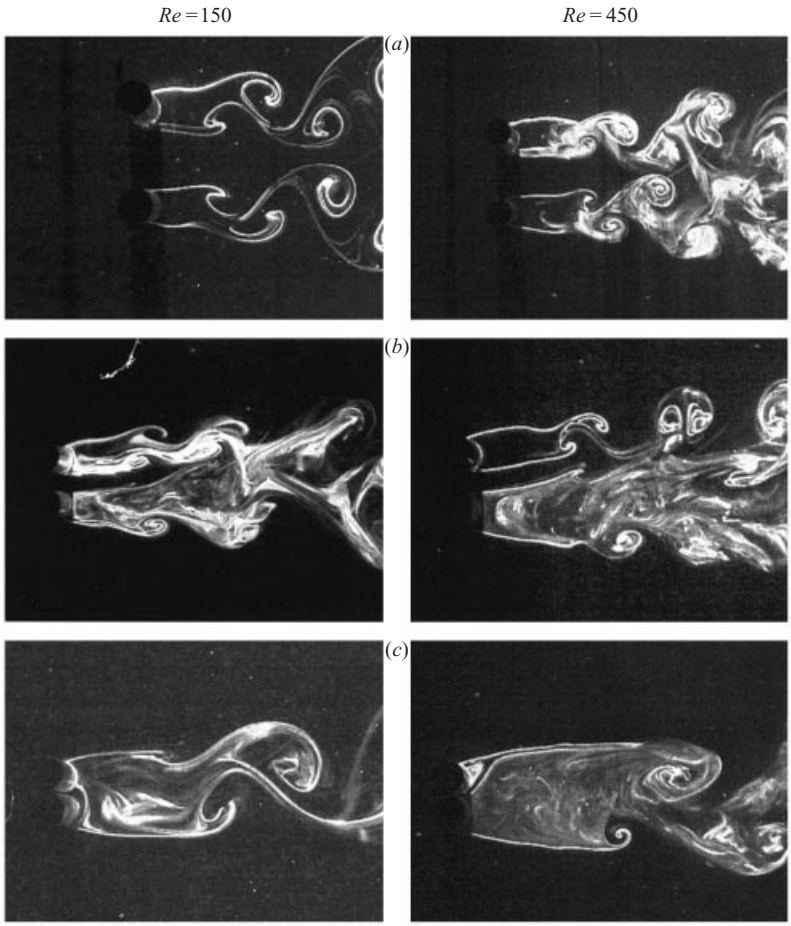

FIGURE 6. Laser-illuminated flow visualization in the water tunnel behind two side-by-side cylinders. Flow is from left to right. (*a*) $T/d = 300$, (*b*) 1.70, (*c*) 1.13.

the free stream, as suggested in figure 4, thus forming a pressure differential on the two sides of each cylinder in the cross-flow direction. This pressure differential could be symmetrical with respect to the mid-point of the gap and could tend to suppress the anti-symmetrical vortex shedding and induce the symmetric behaviour.

$T/d = 1.7$: Typical photographs of the near-wake flow (figure 6*b*) from flow visualization in the laminar and turbulent flow regimes indicate a deflected gap flow between the two cylinders, thus forming one narrow and one wide wake. The results are consistent with those for $T/d = 1.5 \sim 2.0$ previously reported (Spivack 1946; Ishigai *et al.* 1972; Bearman & Wadcock 1973; Kamemoto 1976; Kiya *et al.* 1980; Kim & Durbin 1988; Sumner *et al.* 1999).

$T/d = 1.13$: The gap vortices were not observed and most vortices were shed alternately from the free-stream side of the two cylinders, as evidenced in the photographs (figure 6*c*). The photograph at $Re = 450$ further displays a gap flow or bleeding deflected towards the upper cylinder. The deflected bleeding is likely to cause a difference in p_b between cylinders, and thus be responsible for the different C_D (figure 5*b*). It is worth mentioning that flow visualization data did show the symmetric vortex shedding from time to time when the gap flow was not deflected.

3.3. *Spectral characteristics*

$T/d = 3.0$: The spectra $E_{\epsilon y}$ of ϵ_y from Cylinder 1 and 2 at $U_r \approx 19$ for different T/d values are presented in figure 7 along with the spectrum E_u of the simultaneously measured streamwise velocity u. No resonance occurs at this reduced velocity. Here, the focus is on flow-related spectral characteristics, while vibration-related behaviour, such as the prominent peaks in the ϵ_y-spectrum, is discussed in § 4. At $T/d = 3.00$, the u-spectrum (figure 7*a*) yields one major peak at $f_s^* = f_s d/U_\infty = 0.20$ which is the same as the normalized vortex shedding frequency (or Strouhal number) of a single cylinder. This peak is also evident in the strain spectra and it occurs at the same frequency for the two strain spectra presented, thus indicating that the shedding frequency for the two cylinders is identical. The spectral phase shift Φ_{12} at f_s between the ϵ_y signals is generally near $+\pi$ or $-\pi$ (figure 8*a*), implying that the two cylinders move in opposite directions. These results conform to the observation from flow visualization that the vortices are predominantly shed in symmetric pairs or in an anti-phase mode for the two cylinders.

$T/d = 1.7$: The u-spectrum exhibits a broad peak, ranging from 0.08 to 0.20 and centred at $f_s^* = 0.105$ (figure 7*b*). This result seems to indicate a frequency range of vortex shedding. It has been reported previously that the narrow and wide wakes observed in flow visualization were associated with the high and low vortex frequencies, respectively (Spivack 1946; Ishigai *et al.* 1972; Bearman & Wadcock 1973; Kamemoto 1976; Kiya *et al.* 1980; Kim & Durbin 1988; Sumner *et al.* 1999). The ratio of the two frequencies was close to but less than 3 (Kim & Durbin 1988). This is also observed in the present case. The u-spectra for different Re are shown in figure 9. These spectra show a peak at $f^* \approx 0.1$ or 0.31, or peaks at both frequencies. The physics behind the appearance of two different frequencies is not clear; some researchers (Sumner *et al.* 1999; Kim & Durbin 1988) suggested two vortex shedding processes or frequencies. Based on flow visualization at a low Re ($\leqslant 200$), Williamson (1985) proposed that the two frequencies resulted from the existence of harmonic vortex-shedding modes. The present flow visualization in the laminar and turbulent flow regimes suggests another interpretation.

In order to understand the two dominant frequencies observed in the velocity spectra, the flow visualization data were examined in detail. It was noted that vortices were generally shed alternately from both sides of each cylinder, though the gap vortices appeared to be weaker than the outer vortices, which were shed on the free-stream side. Playing back the tape and counting consecutive vortices (about 15 pairs) at $x/d \approx 2$ for a certain period, it was noted that the vortices were formed at about the same frequency from the two cylinders. For example, at $Re = 450$, f_s^* was about 0.11 for the lower cylinder and 0.126 for the upper. Similar results were obtained for other Re. This raises the question of why the hot wire measured two frequencies and the ratio of the two frequencies was about 3. Sequential photographs at $Re = 450$ are shown in figure 10. The two rows of vortices in the narrow wake appear squeezed by the wide wake so that their lateral spacing is very small. Initially (figure 10*a–c*), the longitudinal spacing between two vortices in the narrow wake, as marked by arrows, is large. However, figures 10(*c*) and 10(*d*) show a reduced spacing between the vortices, suggesting that the convection velocity of the outer vortex was smaller than that of the gap vortex, which was possibly carried by the gap flow jet with a higher mean velocity (Sumner *et al.* 1999). As a result, the two opposite-sign vortices were engaged in a pairing process (figure 10*d–f*). On the other hand, the gap vortex shed from the lower cylinder, also marked by an arrow, appears pushed into close contact with the pairing vortices by the widening wake. Note that the pairing

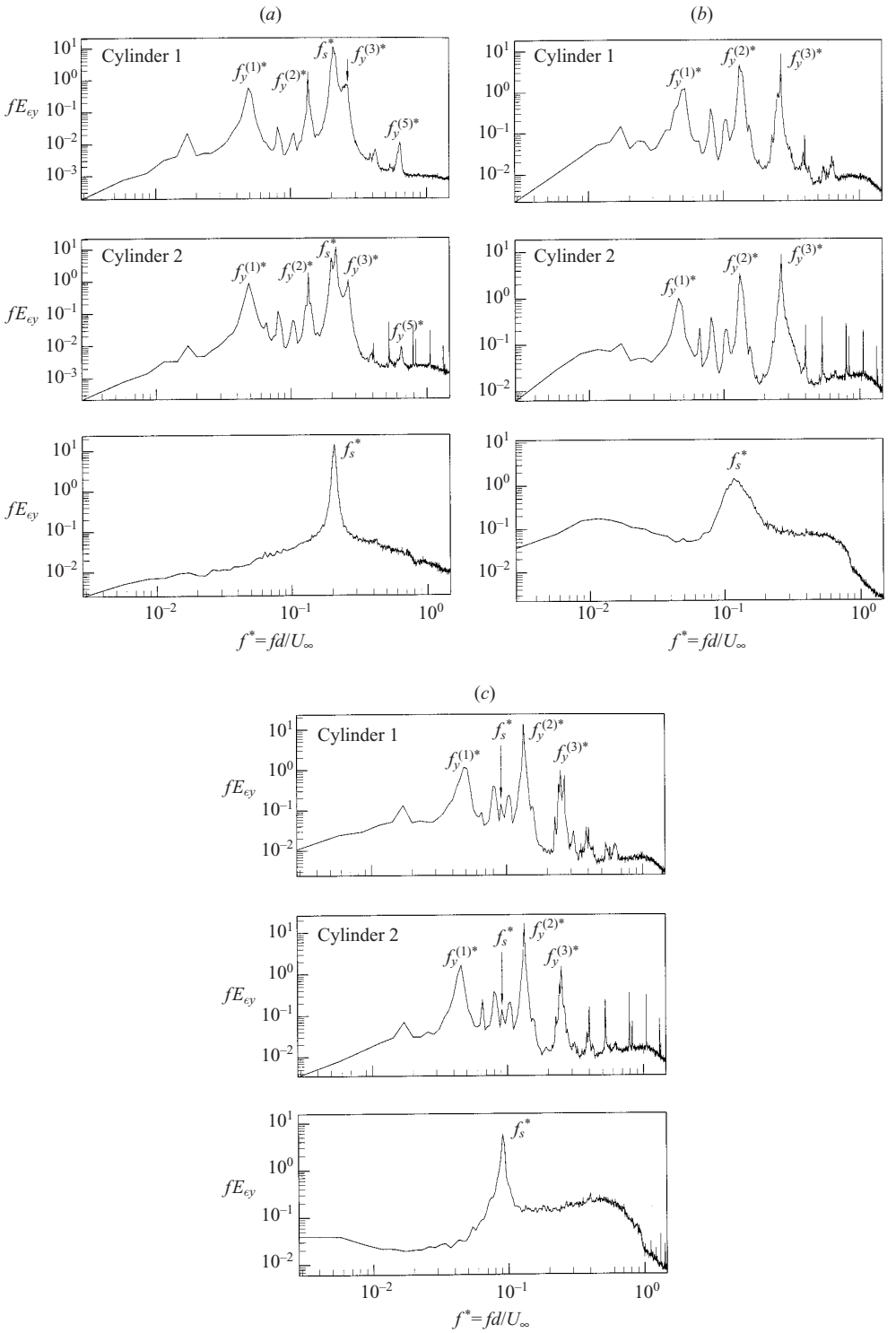

FIGURE 7. Power spectra $fE_{\epsilon y}$ (top: Cylinder 1; middle: Cylinder 2) of the strain ϵ_y, and fE_u (bottom) of the streamwise velocity u at the off-resonance condition ($U_r \approx 19$, $Re = 4900$). The hot wire was located at $x/d = 2$ and $y/d = 1.5$. (*a*) $T/d = 3.00$, (*b*) 1.70, (*c*) 1.13.

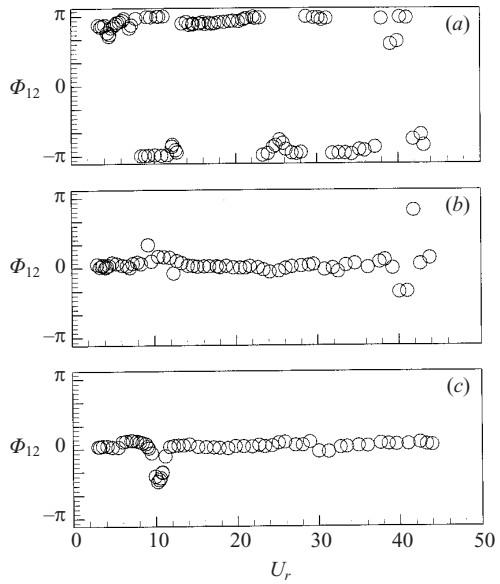

FIGURE 8. Dependence on U_r of the phase shift Φ_{12} at f_s between dynamic strains ϵ_{y1} and ϵ_{y2} measured from the two cylinders. (*a*) $T/d = 3.00$, (*b*) 1.70, (*c*) 1.13.

vortices rotated in opposite directions, acting to 'suck' in the approaching gap vortex (figure 10*d–f*). Because of the small lateral spacing between the three vortices, the hot wire could measure a frequency triple that in the wide wake.

The peak in the *u*-spectrum for $T/d = 1.70$ is considerably less pronounced than that at $T/d = 3.0$. The vortex shedding component is substantially weakened, thus corroborating the earlier suggestion that the vortex strength is reduced at $T/d = 1.70$. This reduction is partly attributable to the interference between cylinders, which could be responsible for a decrease in the drag coefficient (figure 5*b*). However, the ϵ_y-spectra, quite similar for the two cylinders, fail to show a strong presence of the vortex excitation at either f_s^* or $3f_s^*$. The spectral phase shift Φ_{12} between the ϵ_y signals is near zero at $f_s^* = 0.105$ (figure 8*b*) but $+\pi$ or $-\pi$ at $3f_s^*$ (not shown). Therefore, it seems that vortices shed from the two cylinders tend to be in-phase at $f_s^* = 0.105$ for $T/d < 2.0$.

$T/d = 1.13$: When T/d reduces to 1.13, the *u*-spectrum (figure 7*c*) indicates that the vortex shedding frequency is halved, occurring at $f_s^* \approx 0.09$. For such a small transverse spacing, the two cylinders tend to act like a single body and the effective Strouhal number should be $f_s(2.13d)/U_\infty \approx 0.2$, or $f_s d/U_\infty \approx 0.09$. The phase shift Φ_{12} at f_s^* (figure 8*c*) is generally close to zero, indicating that the two cylinders are vibrating in phase in the cross-flow direction. It can be inferred that most of the vortices were shed alternately from the free-stream side of the two cylinders, in conformity to the observation from flow visualization (figure 6*c*). Note that at $U_r = 11$, Φ_{12} drifts away from zero, displaying a valley. Since $f_s^* \approx 0.09$ (figure 7*c*), then the first-mode resonance where $f_0^{(1)} \approx f_s$ occurs at $U_r \approx 1/f_s^* \approx 11$. The natural frequencies of the two cylinders are slightly different (table 1). As a result, while the vibration of one cylinder synchronizes with vortex shedding, the other does not. This implies that the two cylinders could respond very differently to the vortex excitation force, thus leading to a phase shift between their vibrations (figure 8*c*).

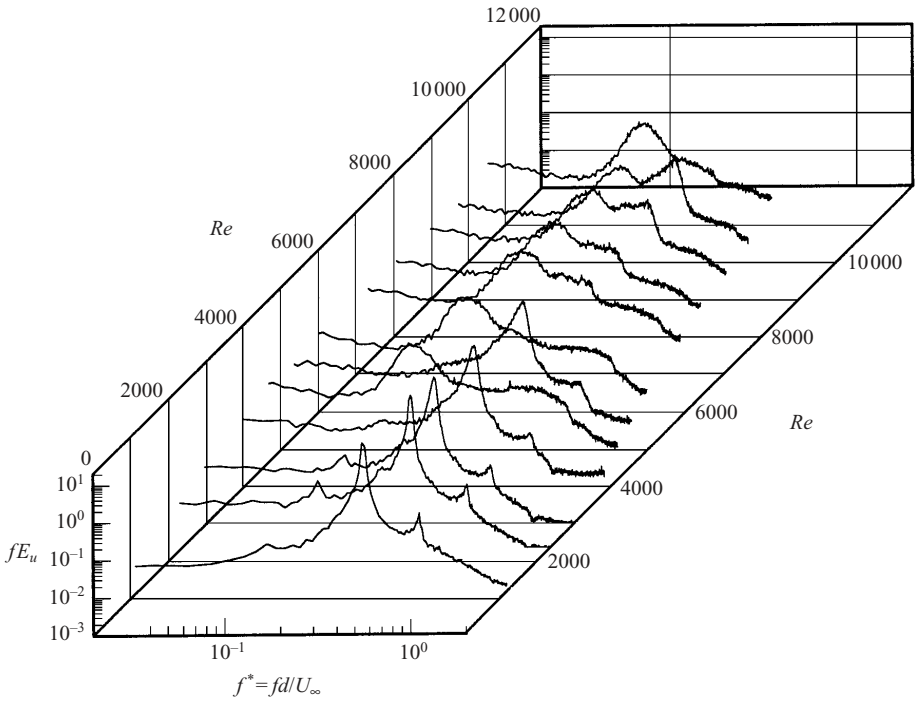

FIGURE 9. Power spectra E_u of u for various Re ($T/d = 1.70$). The hot wire was located at $x/d = 2$ and $y/d = 1.5$.

4. Fluid–structure interactions

4.1. *Spectral behaviour and root-mean-square strain*

The spectrum $E_{\epsilon y}$ (figure 7) of Cylinder 1 exhibits one peak at $f^* \approx 0.049$, irrespective of the transverse spacing. The peak can be identified with the first-mode natural frequency $f_y^{(1)*}$ of the combined fluid–cylinder system for a single cylinder placed in a cross-flow, as verified by the numerical calculation of So *et al.* (2001). Another peak occurs at $f^* \approx 0.264$. The third-mode natural frequency can be estimated from $f_y^{(3)*} = (121/22.4)\ f_y^{(1)*} = 0.265$ (Chen 1987). Therefore, this peak corresponds to the third-mode natural frequency $f_y^{(3)*}$ of the combined fluid–cylinder system. Similarly, the peak at $f^* = 0.135$ is identified with the second-mode natural frequency of the system. The ϵ_y-spectrum from Cylinder 2 closely resembles that from Cylinder 1.

The dependence of $\epsilon_{y,rms}$ and $\epsilon_{x,rms}$ on U_r from the two cylinders is shown in figures 11 and 12, respectively. The r.m.s. values of the measured strain from the two cylinders collapse quite well and generally increase with U_r. At $T/d = 3.00$, $\epsilon_{y,rms}$ displays three peaks at $U_r \approx 4.2$, 12.0 and 26.0, respectively, while $\epsilon_{x,rms}$ shows only one tiny peak at $U_r \approx 26.0$. Note that when $U_r > 33$, $\epsilon_{x,rms}$ increases faster and becomes larger than $\epsilon_{y,rms}$.

The peaks in $\epsilon_{y,rms}$ at $U_r \approx 4.2$, 12.0 and 26.0 (figure 11*a*) can be identified from the spectral analysis with resonance occurring when the vortex shedding frequency is equal to the system natural frequencies $f_y^{(1)}$, $f_y^{(2)}$ and $f_y^{(3)}$, respectively. While the peak at $U_r \approx 12$ is barely identifiable, the one at $U_r \approx 26$ is most prominent. The simultaneously measured $E_{\epsilon y}$ from the two cylinders at $U_r \approx 26$ along with E_u are presented in figure 13. The most prominent peak in $E_{\epsilon y}$ occurs at $f_y^{(3)*} \approx 0.2$, which coincides with f_s^*, as evidenced in E_u (figure 13*c*). The occurrence of resonance is

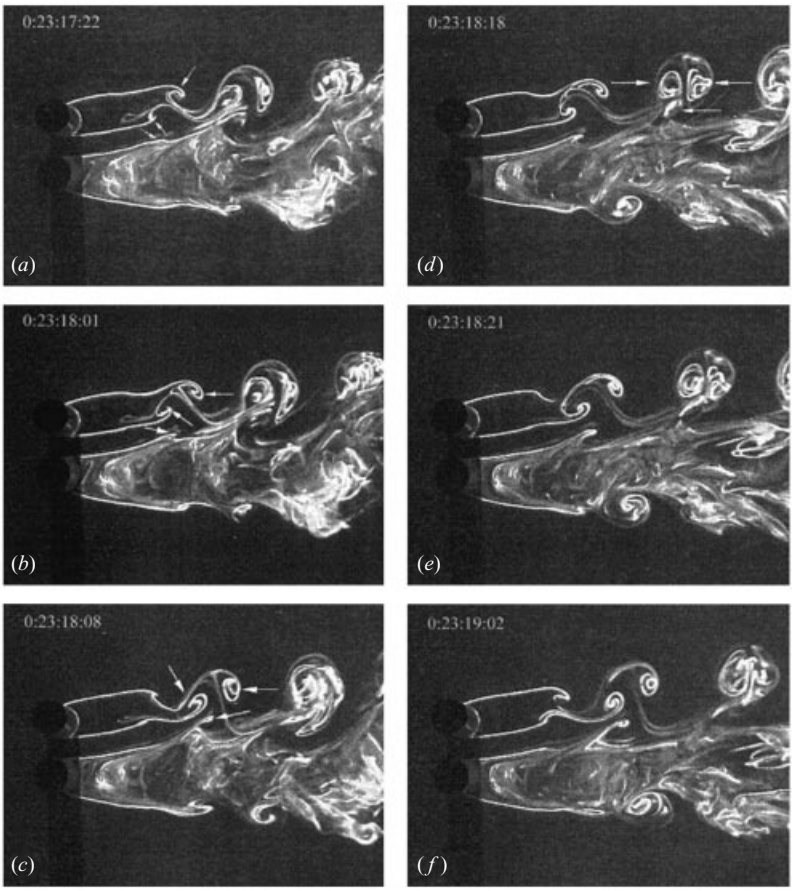

FIGURE 10. Sequential photographs from laser-illuminated flow visualization ($T/d = 1.70$, $Re = 450$).

responsible for this prominent peak in $E_{\epsilon y}$ and hence that at $U_r \approx 26$ in $\epsilon_{y,rms}$. Similarly, the peaks at $U_r \approx 4.2$ and 12 in $\epsilon_{y,rms}$ could be identified with the resonance corresponding to the first- and second-mode natural frequencies of the fluid–cylinder system, respectively.

The observation that the peak at $U_r \approx 26$ is far more pronounced than the others may not be surprising. First, resonance corresponding to $f_y^{(3)}$ occurs at a higher U_r. Flow excitation energy, which is proportional to U_r^2, is therefore much higher. Secondly, it will be seen later in §4.3 that the deduced effective damping ratio, the sum of the structural and fluid damping ratio, corresponding to $f_y^{(3)}$ is appreciably smaller than that corresponding to $f_y^{(1)}$ or $f_y^{(2)}$. This implies that the energy dissipation, when resonance occurs at $f_s = f_y^{(3)}$, is smallest. Thirdly, the fifth harmonic of $f_y^{(1)*}$ (≈ 0.0394) is 0.197 and is very close to $f_s^* = 0.2$. This could feed additional energy to the resonance phenomenon. These three effects combined could lead to a violent vibration or instability at $f_y^{(3)}$ (figure 11*a*). This observation suggests that structural flexibility plays a significant role in the dynamic analysis. In practice, all structures are flexible; however, structural flexibility has so far been ignored in most previous studies.

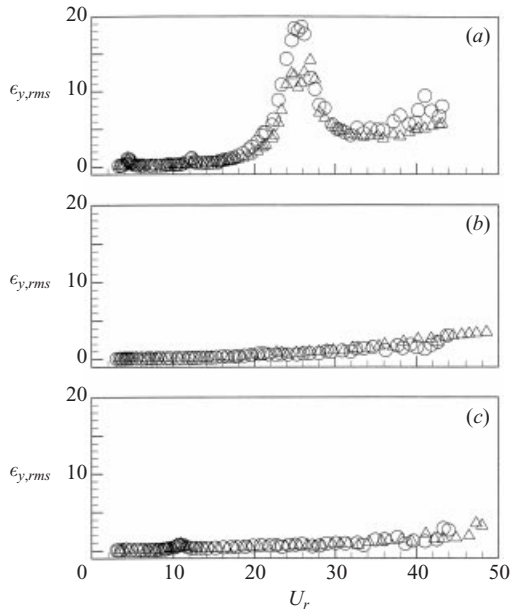

FIGURE 11. Variation of $\epsilon_{y,rms}$ with U_r at various spacing ratios: (*a*) $T/d = 3.00$; (*b*) 1.70; (*c*) 1.13. ◯, Cylinder 1; △, Cylinder 2.

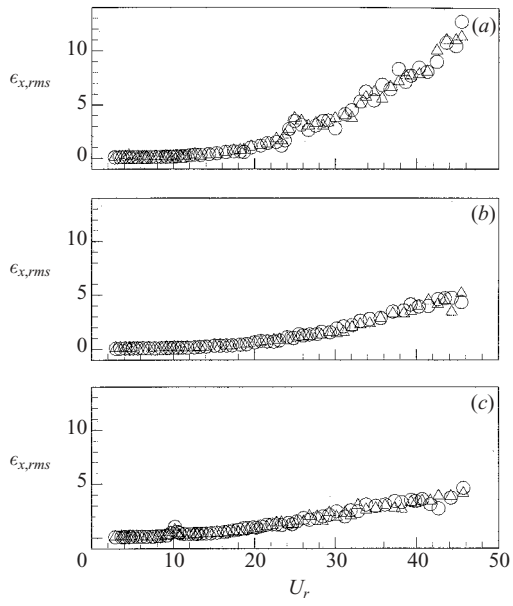

FIGURE 12. Variation of $\epsilon_{y,rms}$ with U_r at various spacing ratios: (*a*) $T/d = 3.00$; (*b*) 1.70; (*c*) 1.13. ◯, Cylinder 1; △, Cylinder 2.

Consequently, resonance occurring at $U_r \approx 5$ has been extensively investigated, while instability corresponding to $f_y^{(3)}$ has been largely overlooked.

As T/d reduces to 1.70, the $\epsilon_{y,rms}$ values decrease considerably for both cylinders; resonance does not appear to occur at all. In this case, vortices shed from both cylinders are very weak, as seen earlier from the *u*-spectrum. Accordingly, structural

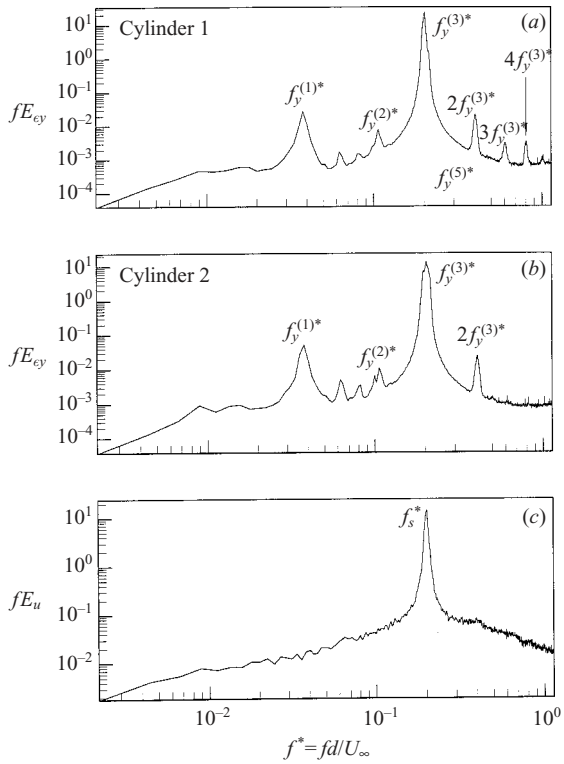

FIGURE 13. Power spectra $fE_{\epsilon y}$ ((*a*) Cylinder 1; (*b*) Cylinder 2) of the strain ϵ_y and fE_u (*c*) of the streamwise velocity u at $U_r \approx 26$ where the third-mode resonance occurs ($T/d = 3.00$). The hot wire was located at $x/d = 2$ and $y/d = 1.5$.

vibrations are impeded, even at the occurrence of resonance. This observation is in marked contrast with that at $T/d = 3.00$. The difference is consistent with the observation from the measured spectra, which exhibited a weakening vortex shedding component at $T/d = 1.70$ (figure 7*b*), compared with that at $T/d = 3.00$ (figure 7*a*). At $T/d = 1.13$, only one peak in $\epsilon_{y,rms}$ and $\epsilon_{x,rms}$ is observed at $U_r \approx 11$ because of the first-mode resonance. The third-mode resonance is expected to occur near $U_r \approx (121/22.4)11 = 59.4$, which is beyond the present measurement range, and therefore cannot be observed in figure 11(*c*).

4.2. *Natural frequencies of the fluid–cylinder system*

The natural frequency $f_y^{(1)}$, identified in figure 7(*a*), of the fluid–cylinder system associated with Cylinder 1 is 101 Hz at $T/d = 3.00$. This frequency changes to 103.3 Hz at $T/d = 1.70$ (figure 7*b*) and 104.7 Hz at $T/d = 1.13$ (figure 7*c*). Note that the mounting of Cylinder 1 was unchanged throughout the experiments. Therefore, $f_y^{(1)}$ should remain fairly constant. Furthermore, the spectra were deduced using a conventional FFT program; the frequency resolution is fixed by the sampling rate and the record length used in the FFT calculation. It is estimated to be 0.35 Hz. In view of these factors, the variation of $f_y^{(1)}$ noted above cannot be attributed to experimental or calculation errors.

The dependence of $f_y^{(1)}/f_o^{(1)}$ in the cross-flow direction on T/d and U_r is shown in figure 14. The linear model in the figure refers to the prediction based on a set of linear partial differentiation equations, as detailed in § 5. Generally, $f_y^{(1)}/f_0^{(1)}$ rises

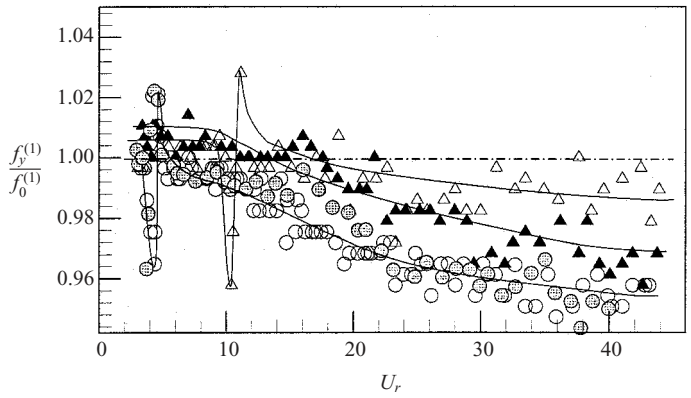

FIGURE 14. Variation of the cross-flow $f_y^{(1)}$ with T/d and U_r. Cylinder 1. △, $T/d = 1.13$; ▲, 1.70; ○, 3.00; ●, single cylinder; –•–, linear model. The solid line indicates the trend.

with decreasing T/d. This is more appreciable when $U_r > 14$. A number of factors could alter the natural frequency of the system other than the repulsive force between the cylinders. As a first-order approximation, a spring–damper–mass model can be used to model the fluid–cylinder system. Both fluid and structure contribute to the system mass, stiffness and the damping ratio. A rise (figure 5*a*) in the repulsive force as the cylinders approach each other is equivalent to an increase in fluid rigidity. Alternatively, from a different perspective, an increasing repulsive force between two cylinders could be associated with a tensile axial loading on the cylinder, which was fix-supported at both ends, and subsequently increased the structural rigidity (Weaver, Timoshenko & Young 1989). As a result, the system natural frequency might increase. This has been qualitatively verified based on the measured lift data. Added mass is another factor that may change the natural frequency of the system. Chen (1987) calculated the added mass on two side-by-side cylinders in a cross-flow and found that, in the range of $1.13 < T/d < 4$, the added mass increases as T/d decreases, thus contributing to a decrease in the system natural frequency. The system natural frequency may also be affected by the non-linear fluid damping. This effect is however not well understood and so makes it difficult to estimate quantitatively the contribution from each factor to the variation in $f_y^{(1)}/f_0^{(1)}$. On the other hand, $f_x^{(1)}/f_0^{(1)}$ in the inline direction appears to decrease for $U_r > 12$ (the corresponding Re is 2900) as T/d reduces (figure 15). Again, this could be the combined effect of varying system mass, stiffness and damping ratios with T/d.

The values of $f_y^{(1)}/f_0^{(1)}$ and $f_x^{(1)}/f_0^{(1)}$ appear to slowly decrease as U_r increases. For the purpose of comparison, the fluctuating displacement data of an isolated elastic cylinder in a cross-flow (Zhou *et al.* 1999) were also analysed. The deduced $f_y^{(1)}/f_0^{(1)}$ is included in figure 14, which exhibits a behaviour similar to the two-cylinder case. It is therefore conjectured that the observation is not directly related to the interference between cylinders but rather to the fluid–cylinder interaction. A linear analysis of the combined fluid–cylinder system in § 5 indicates that a varying fluid damping, as U_r, increases, could be responsible for the slowly evolving system natural frequency.

It is interesting to note that, when resonance occurs near $U_r \approx 4.2$ for $T/d = 3.00$ and $U_r \approx 11.0$ for $T/d = 1.13$, $f_y^{(1)}/f_0^{(1)}$ falls off sharply and then rises rapidly away from resonance. The variation ranges between 6% and 10% of $f_0^{(1)}$. For Cylinder 2, the dependence of $f_y^{(1)}/f_0^{(1)}$ on U_r (not shown) is quite similar to that presented

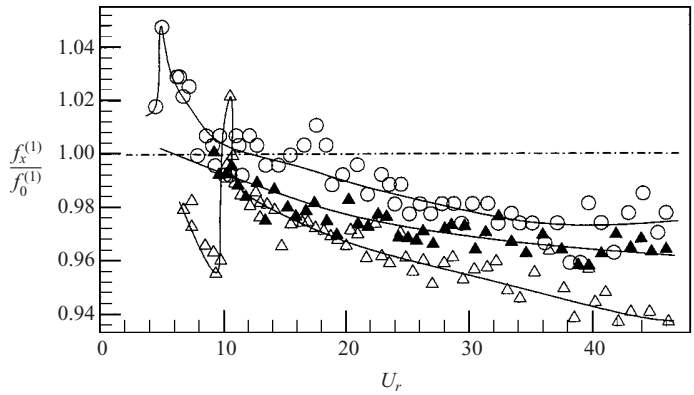

FIGURE 15. Variation of the inline $f_x^{(1)}$ with U_r. Cylinder 1. △, $T/d = 1.13$; ▲, 1.70; ○, 3.00; –•–, linear model. This solid line indicates the trend.

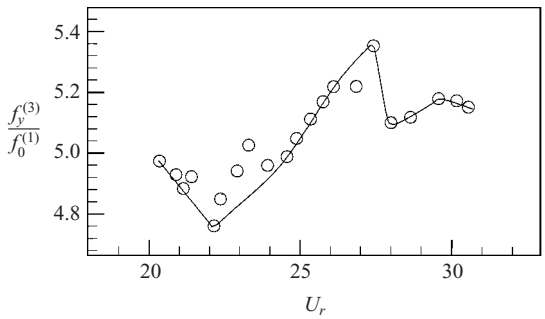

FIGURE 16. Variation of $f_y^{(3)}$ with U_r near resonance. Cylinder 1, $T/d = 3.00$. The solid line indicates the trend.

for Cylinder 1. Price & Paidoussis (1989) measured the free vibration of a cylinder located in a tube bundle in a water cross-flow. Their test cylinder was rigid but flexibly mounted at both ends and $U_r < 10$. They observed that near resonance the system natural frequency (or fluid-elastic natural frequency) decreased initially and then increased rapidly as U_r increases. The mechanism behind the observation was not discussed.

There is no drastic change in $f_y^{(1)}/f_0^{(1)}$ near $U_r = 26.0$ where $\epsilon_{y,rms}$ is largest. As postulated previously, resonance near $U_r = 26.0$ occurs as a result of the coincidence of the vortex shedding frequency with $f_y^{(3)}$. A 10% variation in $f_y^{(3)}/f_0^{(1)}$ between $U_r = 21$ and 31 is clearly shown in figure 16. The observation further corroborates the earlier conjecture that the major mechanism behind the instability, i.e. the prominent peak at $U_r \approx 26.0$, is the resonance of the vortex shedding frequency with $f_y^{(3)}$. The variation of $f_y^{(3)}/f_0^{(1)}$ is similar to that of $f_y^{(1)}/f_0^{(1)}$ near $U_r = 4.2$ for $T/d = 3.00$ or $U_r = 11$ for $T/d = 1.13$.

It is known that when a structure is forced to vibrate in a cross-flow, a lock-in phenomenon occurs when the vortex shedding frequency coincides with the frequency of the imposed excitation force. In free vibration, however, it is the vortex shedding that excites the structure. Therefore, the vortex-induced force dominates. This force has a dominant frequency equal to that of vortex shedding. In the $T/d = 3.0$ case, the ϵ_y-spectra for $U_r = 17$–35 indicate that the third-mode natural frequency varies near resonance; the variation appears to be dictated by the vortex shedding frequency

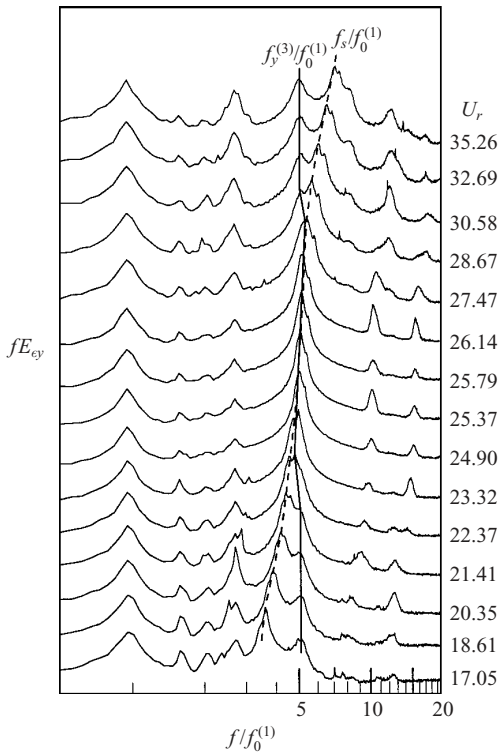

FIGURE 17. Power spectra $fE_{\epsilon y}$ of the strain ϵ_y for varying U_r, $T/d = 3.00$, Cylinder 1. The solid line highlights the trend.

(figure 17). To highlight this point, figure 18 compares the variation of $f_s/f_0^{(1)}$ with that of $f_y^{(3)}/f_0^{(1)}$ (figure 18*a*) and $f_y^{(1)}/f_0^{(1)}$ (figure 18*b*) near resonance. At $U_r = 20.4$, $f_s/f_0^{(1)}$ and $f_y^{(3)}/f_0^{(1)}$ are close enough to interact with each other and resonance starts to occur. Influenced by the relatively small value of $f_s/f_0^{(1)} = 4.2$, $f_y^{(3)}/f_0^{(1)}$ drops from 4.98 to approach $f_s/f_0^{(1)}$. Note that $f_s/f_0^{(1)}$ remains linear with respect to U_r, implying that $f_y^{(3)}$ has little influence on f_s. Such interplay between f_s and $f_y^{(3)}$ continues until they are identical or synchronize at $U_r = 24.6$. The system tends to maintain synchronization. As $f_s/f_0^{(1)}$ increases with increasing U_r, $f_y^{(3)}/f_0^{(1)}$ follows $f_s/f_0^{(1)}$ until eventually $f_s/f_0^{(1)}$ and $f_y^{(3)}/f_0^{(1)}$ are de-coupled from each other at $U_r \approx 26.2$. The interaction between f_s and $f_y^{(1)}$ is quite similar near $U_r = 4.2$ (figure 18*b*) or $U_r = 11$ at $T/d = 1.13$ (not shown). Clearly, vortex shedding dominates the nonlinear interaction between the fluid excitation force and the structural vibration in the free vibration case, thus tuning the natural frequency of the system to the vortex shedding frequency. This observation contrasts with the lock-in phenomenon where the vortex shedding frequency is dictated by the forced vibration frequency of a cylinder.

It is worth pointing out that $f_y^{(3)}$ varies over $U_r \approx 20$–28, whereas $f_y^{(1)}$ varies over $U_r \approx 3.5$–5 only. The difference in the U_r range is probably because the fluid excitation force at $U_r \approx 26$ is far greater than that near $U_r \approx 4.2$. It is foreseeable that the U_r range over which the system natural frequency varies will be even greater in the context of a water flow where the excitation force is much greater.

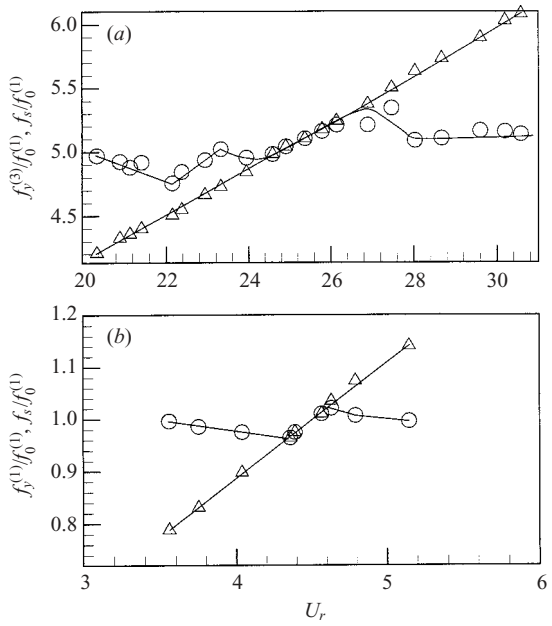

FIGURE 18. Variation of the system's natural frequency (○) and the vortex shedding frequency (△) with U_r around resonance: (*a*) $f_y^{(3)}$ and f_s; (*b*) $f_y^{(1)}$ and f_s. Cylinder 1, $T/d = 3.00$. The solid line indicates the trend.

4.3. *Effective damping ratios*

The effective damping ratio of a fluid–cylinder system is made up of fluid and structural damping. The free vibration of an elastic structure has multiple modes with different natural frequencies and effective damping ratios. This section discusses the behaviour of these modal damping ratios and their dependence on U_r and T/d. The modal damping ratios were calculated from the ϵ_y and ϵ_x signals using the ARMA technique. Interested readers may refer to Mignolet & Red-Horse (1994) for more details.

Figure 19 presents the cross-flow modal damping ratios, $\zeta_{y,e}^{(1)}$, $\zeta_{y,e}^{(2)}$ and $\zeta_{y,e}^{(3)}$, corresponding to the system natural frequencies $f_y^{(1)}$, $f_y^{(2)}$ and $f_y^{(3)}$, respectively. The ratios are calculated from the ϵ_y signals of Cylinder 1. The inline ratios $\zeta_{x,e}^{(1)}$, $\zeta_{x,e}^{(2)}$ and $\zeta_{x,e}^{(3)}$ are given in figure 20. In these figures, the solid line represents the first-mode structural damping ratio.

The values of $\zeta_{y,e}^{(2)}$ and $\zeta_{x,e}^{(2)}$ exhibit relatively large scattering. As shown in figure 11, the resonance corresponding to the second-mode natural frequency of the system is the least violent at $T/d = 3.00$ and fails to occur when $T/d < 3.00$. The ϵ_y-spectrum (not shown) indicates that even when f_s coincides approximately with $f_y^{(2)}$ at $T/d = 1.13$, the peak at $f_y^{(2)}$ does not appear to be more pronounced than that at $f_y^{(1)}$ and $f_y^{(3)}$. It is evident that the excitation for the second mode of vibration is weak, as compared with that for the first or third mode of vibration. This is reasonable. The assumption of two-dimensional flow and a uniform excitation force along the cylinder span leads to symmetry about the mid-span. As a result, the numerical solution cannot admit a second-mode vibration (Wang *et al.* 2000). In a real fluid–cylinder system, however, the vortices shed from the cylinder are not two-dimensional when $Re > 400$ (Bloor 1964; Evangelinos & Karniadakis 1999); their spanwise extent is also limited,

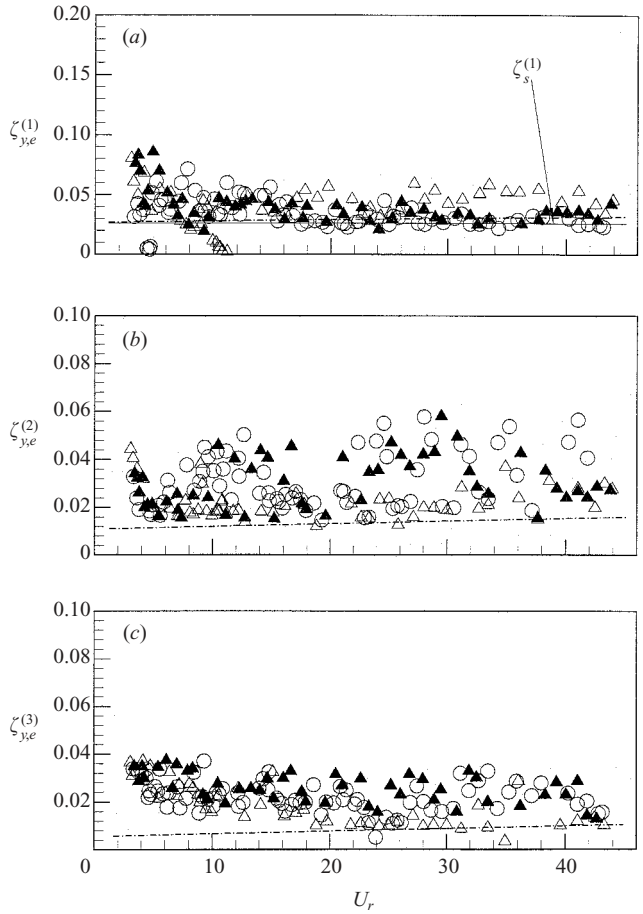

FIGURE 19. Cross-flow effective damping ratios of the fluid–cylinder system: (*a*) $\zeta_{y,e}^{(1)}$; (*b*) $\zeta_{y,e}^{(2)}$; (*c*) $\zeta_{y,e}^{(3)}$. Cylinder 1. △, $T/d = 1.13$; ▲, 1.70; ○, 3.00; –·–, linear model.

typically 1*d* to 3*d* (Zhou & Antonia 1994). This implies a non-uniform excitation force along the cylinder span, thus exciting even-mode vibrations (figures 7 and 13). It is possible that excitation due to the three-dimensionality of the shed vortices is small compared with the two-dimensional excitation due to periodic shedding. Therefore, the even-mode resonance could be much weaker in strength than the odd-mode resonance. Consequently, uncertainty in the estimation of even-mode damping ratios will increase, resulting in much more scattering in the deduced $\zeta_{y,e}^{(2)}$ and $\zeta_{x,e}^{(2)}$.

A few observations can be made based on the results presented in figures 19 and 20. First, the effective damping ratio approaches zero when resonance occurs. Both $\zeta_{x,e}^{(1)}$ and $\zeta_{y,e}^{(1)}$ decrease sharply near $U_r \approx 11$ for $T/d = 1.13$ and near $U_r \approx 4.2$ for $T/d = 3.00$ to a level well below the structural damping ratio. This suggests that the fluid damping ratio is negative at resonance. Note that near $U_r \approx 26$, $\zeta_{y,e}^{(3)}$ instead of $\zeta_{y,e}^{(1)}$ or $\zeta_{y,e}^{(2)}$ dips, in further support of the earlier conjecture that the strongest peak in $\epsilon_{y,rms}$ is mainly due to resonance occurring where f_s coincides with $f_y^{(3)}$.

Secondly, for $T/d = 3.00$, $\zeta_{x,e}^{(1)}$ is generally larger than $\zeta_{y,e}^{(1)}$ in the range $U_r < 8$, implying larger fluid damping. This observation agrees with the finding of Granger *et al.* (1993) for a small flow velocity. Based on a linear assumption that the structural

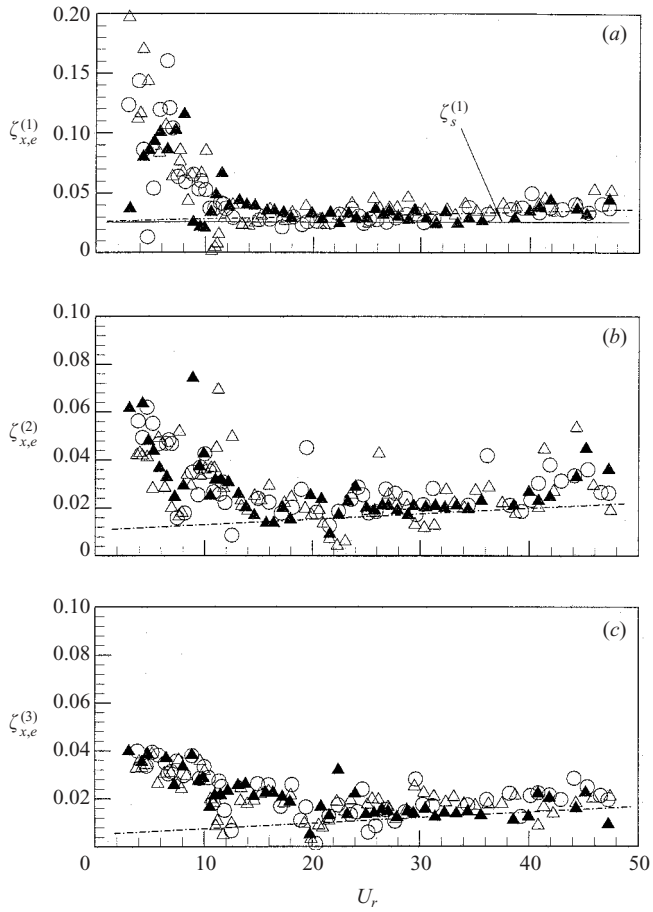

FIGURE 20. Inline effective damping ratios of the fluid–cylinder system: (*a*) $\zeta_{x,e}^{(1)}$; (*b*) $\zeta_{x,e}^{(2)}$; (*c*) $\zeta_{x,e}^{(3)}$. Cylinder 1. △, $T/d = 1.13$; ▲, 1.70; ◯, 3.00; –•–, linear model.

vibration velocity is small relative to the free-stream velocity, Blevins (1994) showed that, for a fluid–cylinder dynamic system, the inline fluid damping is twice that in the cross-flow direction. The analysis is expected to be valid for small U_r only. When $8 < U_r < 15$, the trend is reversed; $\zeta_{x,e}^{(1)}$ becomes smaller than $\zeta_{y,e}^{(1)}$. As U_r further increases, $\zeta_{y,e}^{(1)}$ and $\zeta_{x,e}^{(1)}$ are nearly the same, approximately given by the structural damping ratio. On the other hand, $\zeta_{x,e}^{(2)}$ and $\zeta_{x,e}^{(3)}$ are quite comparable in magnitude with their counterparts in the lift direction, probably due to the relatively small contribution from fluid damping. The behaviour of the damping ratios for $T/d = 1.70$ is quite similar to that for $T/d = 3.00$. However, at $T/d = 1.13$, the fluid damping ratio $\zeta_{y,f}^{(1)} (= \zeta_{y,e}^{(1)} - \zeta_s^{(1)})$ increases significantly, accounting for about one half of the effective damping ratio.

Thirdly, $\zeta_{y,e}^{(3)}$ appears to be the smallest, ranging between 0.01 and 0.03. Blevins (1975) measured the structural damping ratio of a tube and found that the third-mode structural damping ratio was appreciably smaller than the first- and second-mode damping ratios. This may largely account for the relatively small value of $\zeta_{y,e}^{(3)}$ since the fluid damping ratio is small in the present situation. The small $\zeta_{y,e}^{(3)}$ may also contribute to the observation that the third-mode resonance where f_s coincides with $f_y^{(3)}$ is far more violent than the first-mode resonance where f_s approaches $f_y^{(1)}$.

Finally, the effective damping ratios rise, though slowly, as U_r increases beyond 15, apparently resulting from increasing fluid damping.

5. A linear analysis of the fluid–cylinder system

From § 4, it is obvious that variation of the system natural frequencies with U_r exists for an isolated cylinder as well as for two cylinders. Therefore, it could be conjectured that the phenomenon is independent of the interference between cylinders. In view of this and for the sake of theoretical simplicity, an isolated cylinder, fixed at both ends, in a cross-flow is considered in an attempt to seek a dynamic analysis of the fluid–cylinder system. This analysis could provide valuable insight into the mechanism behind the experimental observations.

Let X, Y and Z denote the displacement in the x-, y- and z-directions, respectively. Based on the Euler–Bernoulli beam theory, the displacement field of the cylinder can be written as

$$\begin{aligned} X &= X(z,t), \\ Y &= Y(z,t), \\ Z &= Z_1(x',z,t) + Z_2(y',z,t), \quad x', y' \in [-d/2, d/2], \end{aligned}$$

where $Z_1 = -x'\partial X/\partial z$, $Z_2 = -y'\partial Y/\partial z$. Neglecting damping, the governing equations of the bending vibration, based on Hamilton's principle (Rao 1992), are

$$EI\frac{\partial^4 X(z,t)}{\partial z^4} + \rho_s A\frac{\partial^2 X(z,t)}{\partial t^2} = q_x, \tag{5.1a}$$

$$EI\frac{\partial^4 Y(z,t)}{\partial z^4} + \rho_s A\frac{\partial^2 Y(z,t)}{\partial t^2} = q_y, \tag{5.1b}$$

where ρ_s is the density of the structure, A is the cross-sectional area, q_x and q_y are the flow excitation forces in the x- and y-direction, respectively. When the effects of viscous damping and added mass are considered, (5.1) becomes

$$EI\frac{\partial^4 X(z,t)}{\partial z^4} + c\frac{\partial X(z,t)}{\partial t} + (c_m+1)\rho_s A\frac{\partial^2 X(z,t)}{\partial t^2} = q_x, \tag{5.2a}$$

$$EI\frac{\partial^4 Y(z,t)}{\partial z^4} + c\frac{\partial Y(z,t)}{\partial t} + (c_m+1)\rho_s A\frac{\partial^2 Y(z,t)}{\partial t^2} = q_y, \tag{5.2b}$$

where c is the structural viscous damping coefficient and c_m is the added mass coefficient. The flow excitation forces q_x and q_y are largely dependent on the flow around the cylinder, which is governed by the Navier–Stokes equations,

$$\nabla \cdot \boldsymbol{V} = 0, \tag{5.3}$$

$$\frac{\mathrm{D}\boldsymbol{V}}{\mathrm{D}t} = -\frac{1}{\rho}\nabla p + \nu\nabla^2 \boldsymbol{V}. \tag{5.4}$$

Here, $\mathrm{D}/\mathrm{D}t$ is the material derivative, t is time, $\boldsymbol{V}$ is the instantaneous velocity vector and p is the static pressure. Equations (5.2)–(5.4) are the governing equations for the fluid–cylinder system.

In order to solve (5.2), the flow excitation forces need to be specified. The excitation forces in (5.2) can be decomposed into three components, $q_\beta = \bar{q}_\beta + \tilde{q}_\beta + q'_\beta$, where the overbar, tilde and prime denote the time-mean, periodical and random components

of the fluid force, respectively. The subscript β stands for either the x- or y-direction. Assuming the random fluctuating force q'_β to be negligible, in view of the fact that the vortex shedding excitation is dominant, the other two components can be represented by

$$\bar{q}_x = \tfrac{1}{2}\rho U_\infty d\left[C_D\left(U_{rel} - \tfrac{U_{rel}}{U_\infty}u_{cyl}\right) + C_L\tfrac{U_{rel}}{U_\infty}v_{cyl}\right], \tag{5.5a}$$

$$\tilde{q}_x = \tfrac{1}{2}\rho U_\infty^2 d C'_D \sin\Omega_D t, \tag{5.5b}$$

$$\bar{q}_y = \tfrac{1}{2}\rho U_\infty d\left[C_L\left(U_{rel} - \tfrac{U_{rel}}{U_\infty}u_{cyl}\right) - C_D\tfrac{U_{rel}}{U_\infty}v_{cyl}\right], \tag{5.5c}$$

$$\tilde{q}_y = \tfrac{1}{2}\rho U_\infty^2 d C'_L \sin\Omega_L t. \tag{5.5d}$$

In the above equations, C'_D and C'_L are the fluctuating drag and lift coefficients, $u_{cyl} = \partial X/\partial t$ and $V_{cyl} = \partial Y/\partial t$ are velocities of the cylinder in the x- and y-direction, respectively, Ω_D and Ω_L are the fluctuating drag and lift frequency, respectively, and U_{rel} is the relative velocity between the flow and the cylinder.

The present experimental conditions give rise to the approximation $U_\infty \gg u_{cyl}$ or v_{cyl}. For example, when the third-mode resonance occurs at $U_\infty \approx 16\,\mathrm{m\,s^{-1}}$, u_{cyl} or v_{cyl} is estimated to be of the order of $0.2\,\mathrm{m\,s^{-1}}$, or about $0.012U_\infty$. Consequently, $U_{rel} = \sqrt{v_{cyl}^2 + (U_\infty - u_{cyl})^2} \approx U_\infty - u_{cyl}$, and $(U_{rel}/U_\infty) \approx 1$. For an isolated cylinder, $C_L = 0$. Therefore, the coupled nonlinear equations (5.2) may be decoupled and linearized. Rearranging (5.2) yields the following linear and decoupled partial differential equations:

$$EI\frac{\partial^4 X(z,t)}{\partial z^4} + (c + \rho U_\infty d C_D)\frac{\partial X(z,t)}{\partial t} + (c_m + 1)\rho_s A\frac{\partial^2 X(z,t)}{\partial t^2} = \tfrac{1}{2}\rho U_\infty^2 d(C_D + C'_D \sin\Omega_D t), \tag{5.6a}$$

$$EI\frac{\partial^4 Y(z,t)}{\partial z^4} + (c + \tfrac{1}{2}\rho U_\infty d C_D)\frac{\partial Y(z,t)}{\partial t} + (c_m + 1)\rho_s A\frac{\partial^2 Y(z,t)}{\partial t^2} = \tfrac{1}{2}\rho U_\infty^2 d C'_L \sin\Omega_L t. \tag{5.6b}$$

The system natural frequencies can be obtained by solving the set of homogeneous equations (5.6). Assuming that the general solution of (5.6*a*) is given by

$$X(z,t) = A_x(z)\mathrm{e}^{st}, \tag{5.7}$$

where $A_x(z)$ is a function of z (Weaver *et al.* 1989) and s is a complex coefficient, the shape of the natural mode of vibration in the drag direction can be determined. Substituting (5.7) into (5.6*a*), the following characteristic equation can be deduced from the homogeneous equation:

$$EI\frac{\partial^4 A_x(z)}{\partial z^4} + (sc_x + Ms^2)A_x(z) = 0, \tag{5.8}$$

where $M = (c_m + 1)\rho_s A$ is the sum of the cylinder mass and added mass per unit length and

$$c_x = c + \rho U_\infty d C_D \tag{5.9}$$

is the viscous damping coefficient of the fluid–cylinder system in the drag direction.

The second term on the right-hand side of (5.9) is the drag-induced fluid damping coefficient.

Noting that the boundary conditions of the cylinder fixed at both ends are given by

$$A_x(0) = A_x(l) = \frac{\partial A_x}{\partial z}\Big|_{z=0} = \frac{\partial A_x}{\partial z}\Big|_{z=l} = 0,$$

where l is the length of the cylinder, the eigenvalues of (5.8) can be solved to give the following frequency equation (James *et al.* 1994):

$$\cos r_1 l \cosh r_1 l = 1, \tag{5.10}$$

where $r_1 = \sqrt[4]{-(Ms^2 + c_x s)/EI}$. Applying a method similar to that used by Weaver *et al.* (1989) to (5.10), its roots can be approximated with satisfactory accuracy by the following formula;

$$r_1 l \approx \frac{2n+1}{2}\pi, \quad n = 1, 2, \ldots. \tag{5.11}$$

Assuming weak damping and substituting the solution of (5.11) in terms of s into (5.7) yields

$$X(z,t) = A_x(z)\mathrm{e}^{-c_x/2M}(C_1 \sin(\sqrt{4MEI((2n+1)\pi/2l)^4 - c_x^2}/2M)t + C_2 \cos(\sqrt{4MEI((2n+1)\pi/2l)^4 - c_x^2}/2M)t), \tag{5.12}$$

where C_1, and C_2 are constants determined from the initial condition. Evidently, the natural frequencies are given by

$$f_x^{(n)} = \frac{\omega_x^{(n)}}{2\pi} = \frac{\sqrt{4MEI((2n+1)\pi/2l)^4 - c_x^2}}{4\pi M}, \tag{5.13}$$

where n denotes the nth mode of vibration.

Neglecting damping, i.e. setting $c_x = 0$, (5.13) is reduced to

$$f_0^{(n)} = \left(\frac{2n+1}{3}\right)^2 f_0^{(1)}, \quad n = 1, 2, \ldots, \tag{5.14}$$

where $f_0^{(1)} = \frac{9}{8}\pi\sqrt{EI/Ml^4}$ is the first-mode natural frequency of the cylinder without considering damping. After some algebra, (5.13) can be rewritten as

$$f_x^{(n)} = f_0^{(n)}\sqrt{1 - (\zeta_{x,e}^{(n)})^2}, \quad n = 1, 2, \ldots, \tag{5.15}$$

where the viscous damping ratio or damping factor is given by

$$\zeta_{x,e}^{(n)} = \frac{c_x}{2M\omega_0^{(n)}} = \frac{c_x}{4\pi M f_0^{(n)}}, \quad n = 1, 2, \ldots. \tag{5.16}$$

Considering (5.9), $\zeta_{x,e}^{(n)}$ may be decomposed as

$$\zeta_{x,e}^{(n)} = \zeta_s^{(n)} + \zeta_{x,f}^{(n)}, \tag{5.17}$$

where

$$\zeta_s^{(n)} = \frac{c}{4\pi M f_0^{(n)}} \tag{5.18}$$

originates from the structural damping and

$$\zeta_{x,f}^{(n)} = \frac{9C_D}{4\pi(2n+1)^2 M^*} U_r \tag{5.19}$$

is the drag-induced inline fluid damping ratio. The mass ratio M^* in (5.19) is defined by $M/\rho d^2$. Similarly, the cross-flow natural frequencies of the system are given by

$$f_y^{(n)} = f_0^{(n)}\sqrt{1-(\zeta_{y,e}^{(n)})^2}. \tag{5.20}$$

The cross-flow viscous damping ratio $\zeta_{y,e}^{(n)}$ is given by

$$\zeta_{y,e}^{(n)} = \zeta_s^{(n)} + \zeta_{y,f}^{(n)}, \tag{5.21}$$

where

$$\zeta_{y,f}^{(n)} = \frac{9C_D}{8\pi(2n+1)^2M^*}U_r \tag{5.22}$$

is the drag-induced cross-flow fluid damping ratio. The drag-induced fluid damping ratios (5.19 and 5.22) obtained here are consistent with those given in Chen (1987).

Equations (5.14)–(5.22) describe the behaviour of the system natural frequencies and viscous damping ratios for a linear fluid–cylinder dynamic system. The two parameters are related. Evidently, the fluid damping ratios and the system natural frequencies depend on the dimensionless parameters M^*, C_D and U_r. With M^* fixed and little variation in C_D, the effect of U_r becomes significant. To the lowest order, the model is qualitatively consistent with experimental observation. First, as the structural mode n increases, the natural frequencies (5.14) of the cylinder increase and the corresponding structural damping ratios (5.18) decrease. On the other hand, the fluid damping ratios are virtually independent of the structural mode because the effects of n and U_r cancel out each other ((5.19) or (5.22)). For instance, at the first-mode resonance ($n = 1$), $(2n+1)^2 = 9$ and $U_r \approx 5$. At the third-mode resonance ($n = 3$), $(2n+1)^2 = 49$ and $U_r \approx 26$. The ratio $U_r/(2n+1)^2$ remains almost unchanged. The resultant effective damping ratios therefore decrease for a higher vibration mode. The model prediction (figures 19 and 20) agrees reasonably well with the experimental effective damping ratios at $T/d = 3.00$, in particular in the streamwise direction for $U_r > 10$. Secondly, as U_r increases, the drag-induced fluid damping ratios ((5.19) and (5.22)) increase. However, the contribution from fluid damping to the effective damping ratios is small in the present context. This could explain why the effective damping ratios (figures 19 and 20) increase slowly when $U_r > 15$, which is consistent with the observation that the measured effective damping ratios are quite comparable in the inline and cross-flow directions. Thirdly, since fluid damping is increasing, albeit only slowly, with increasing U_r, the system natural frequencies ((5.15) and (5.20)) will decrease, as seen in the measurements. The linear model of the dynamic system cannot predict the sharp variation in the measured natural frequencies around resonance, because the nonlinear fluid–cylinder interactions are expected to be strong near resonance. Furthermore, the model predictions of $f_x^{(1)}$ and $f_y^{(1)}$, though qualitatively consistent with measurements, deviate from experimental data at $T/d = 3.00$ (figures 14 and 15). The following analysis of the dimensionless governing equations of the fluid–cylinder system indicates that dimensionless parameters other than U_r, C_D and M^* may also play a role in the behaviour of $f_x^{(n)}$ and $f_y^{(n)}$.

The characteristic length and velocity scales are taken to be d and U_∞, respectively, (5.3), (5.4) and the vector form of (5.6) can be made dimensionless by these scales, so that $X^* = X/d$, $Y^* = Y/d$, $z^* = z/d$, $t^* = tU_\infty/d$, $\mathrm{D}/\mathrm{D}t^* = (U_\infty/d)\mathrm{D}/\mathrm{D}t$, $\nabla^* = d\nabla$ and $p^* = p/\rho U^2$. The dimensionless equations can be written as

$$\nabla^* \cdot \boldsymbol{V}^* = 0, \tag{5.23a}$$

$$\frac{\mathrm{D}\boldsymbol{V}^*}{\mathrm{D}t^*} = -\nabla^* p^* + \frac{1}{\mathrm{Re}}\nabla^{*2}\boldsymbol{V}^*, \tag{5.23b}$$

$$\frac{l^{*4}}{U_r^2}\frac{\partial^4 \boldsymbol{w}^*}{\partial z^*} + \frac{9\pi^3(2n+1)^2}{16U_r}\zeta_e\frac{\partial \boldsymbol{w}^*}{\partial t^*} + \frac{81\pi^2}{64}\frac{\partial^2 \boldsymbol{w}^*}{\partial t^{*2}} = \frac{81\pi^2}{128M^*}\boldsymbol{C}_f. \tag{5.23c}$$

Here, the aspect ratio is $l^* = l/d$, the dimensionless displacement vector is $\boldsymbol{w}^* = \{X^*, Y^*\}$, the dimensionless force vector is $\boldsymbol{C}_f = \{C_{x,f} = C_D + C'_D \sin\Omega_D t, C_{y,f} = C'_L \sin\Omega_L t\}$ and the effective damping ratios are $\zeta_e = \zeta_{x,e}^{(n)}$ in the x-direction and $\zeta_{y,e}^{(n)}$ in the y-direction.

There is a total of eight dimensionless parameters in this set of fluid–cylinder governing equations: Re, U_r, l^*, M^*, $C_{x,f}$ and $C_{y,f}$, ζ_e, including $\zeta_s^{(n)}$ and $\zeta_{x,f}^{(n)}$ or $\zeta_{y,f}^{(n)}(\zeta_{x,f}^{(n)} = 2\zeta_{y,f}^{(n)})$. In each direction, there are six dimensionless parameters. It is obvious that if the fluid–cylinder interaction problem is to be understood thoroughly, all the parameters need to be investigated systematically. In the present investigation, the cylinder and boundary conditions are fixed. Therefore, l^*, M^* and $\zeta_s^{(n)}$ are constant. Furthermore, with $f_0^{(1)}$ fixed, varying Re is equivalent to changing U_r. The structural responses are therefore determined by three parameters, i.e. U_r, $\zeta_{x,f}^{(n)}$ or $\zeta_{y,f}^{(n)}$ and $C_{x,f}$ or $C_{y,f}$, which is evident from (5.16)–(5.22).

The issue is raised of whether fluid damping has been adequately accounted for. Fluid damping is very difficult to evaluate accurately. In the present analysis, only a linear drag-induced fluid damping (5.19) and (5.22) was considered. Most likely, this is inadequate to model fluid damping, because fluid–structure interaction is by nature a nonlinear function of fluid velocity and structural motion. Among the available models, the fluid damping force $F_f = h_f|\dot{w}|^\alpha w$ with $0 \leqslant \alpha \leqslant 1$, where w is the structural vibration displacement and h_f is a positive constant that is a function of the cylinder geometry and fluid properties, is most appropriate for moderate Re (Nayfeh & Mook 1995). The equation points to an effect of the force coefficient on fluid damping due to the fact that the force and vibration amplitude are directly correlated. If this is incorporated into (5.2), the nonlinear damping implied in the above equation could significantly increase the difficulty in solving the governing equations for the system natural frequencies. Evidently, the linear approximation to the nonlinear fluid damping would affect the correct calculation of the system natural frequencies. The nonlinear fluid damping effect, which could not be quantified here, is most likely to contribute to the discrepancy between experimental observation and the linear model prediction (figures 14 and 15). In the presence of a neighbouring cylinder, another parameter T/d is also important. This parameter, not considered in the derivation of (5.7)–(5.11), could also be partially responsible for the discrepancy.

6. Conclusions

Fluid–structure interactions of two freely vibrating elastic cylinders in a cross-flow have been experimentally investigated. The following conclusions can be drawn.

1. Vortex formation and its evolution around the cylinders have been examined. The spectral phase shift Φ_{12} between the vibrations of the two cylinders is $\pm\pi$ at $T/d = 3.0$. This observation is consistent with previously reported results (Ishigai *et al.* 1972; Bearman & Wadcock 1973) that vortex pairs are symmetrically formed and shed from the two cylinders for a sufficiently large transverse spacing. Accordingly, the two vortex streets immediately behind the cylinders are predominantly in the anti-phase mode. Furthermore, this finding is found to be independent of Re. As T/d reduces to 1.7, one narrow and one wide wake were observed and the corresponding normalized

dominant frequencies, as seen from velocity spectra, were 0.31 and 0.105, respectively. Flow visualization results suggest that vortices might be shed from both sides of each cylinder at the same frequency, i.e. $f_s^* \approx 0.1$. The two vortices across the narrow wake displayed different convection velocity and subsequently underwent pairing. The two counter-rotating pairing vortices further acted to 'suck' in the gap vortex in the wide wake generated by the other cylinder. Consequently, the three vortices merged and had a small lateral spacing, resulting in a prominent peak in the velocity spectra at $f^* \approx 0.3$. Further investigation is needed to verify this interpretation. At $T/d = 1.13$, Φ_{12} is generally near zero, indicating a dominance by the alternate vortex shedding, though symmetric shedding is seen from the flow visualization data from time to time.

2. Vibration characteristics of the elastic cylinders contrast distinctly with those of rigid ones. The instability of a rigid circular cylinder occurs at the first-mode resonance only. For the $T/d = 3.0$ elastic cylinder case, the present measurements indicate the occurrence of first-, second- and third-mode resonance. The third-mode resonance is far more violent due to the combined effect of higher flow energy, smaller effective damping ratio, and synchronization of vortex shedding with the fifth harmonic of $f_y^{(1)}$. This finding points to the significant role structural flexibility plays in structural instability, which has been overlooked in most previous studies. The inline vibration appears to be far less violent for the third-mode resonance than the cross-flow one.

3. The natural frequencies of the combined fluid–cylinder system change as a result of fluid–structure interactions. First, the natural frequencies of the system experience a rather sudden variation, up to 10%, near resonance. The variation always displays the pattern of a dip followed by a rise. In the free vibration case, vortex shedding dominates the nonlinear interaction between the fluid excitation force and the structural vibration. As a result, when the vortex shedding and system natural frequency components approach each other, the system natural frequency is modified so as to adapt to the vortex shedding frequency. The observation contrasts with the lock-in phenomenon where the vortex shedding frequency is tuned to the forced vibration frequency of a cylinder. Secondly, the cross-flow natural frequencies of the system increase when the transverse spacing ratio is decreased. Presumably, the fluid–cylinder system may be modelled by a mass–spring–damper system; both fluid and structures contribute to the stiffness and damping. The observed increase in the repulsive force between the cylinders as they approach each other could be seen as an increase in fluid stiffness, thus causing a rise in the cross-flow natural frequency of the system. Thirdly, the natural frequencies of the fluid–cylinder system appear to decrease, albeit slowly, as U_r increases. The observation, which also persists for the single-cylinder case, does not seem to depend on the interference between cylinders. A linear analysis of an isolated cylinder in a cross-flow has been conducted. The analysis suggests that fluid damping increases with U_r, thus causing a decrease in the system natural frequencies. Theoretical analysis further indicates that, in addition to the reduced velocity and fluid damping ratios, force coefficients and the spacing ratio also affect the natural frequencies. This, along with the nonlinearity of the fluid–cylinder system, may account for the deviation between the linear analysis and experimental data.

4. The effective damping ratios of the cylinders with a relatively large mass ratio have been characterized. The values of $\zeta_{y,e}^{(1)}$ approach zero when resonance occurs near $U_r \approx 11$ for $T/d = 1.13$ and near $U_r \approx 4.2$ for $T/d = 3.00$, so does $\zeta_{y,e}^{(3)}$ near $U_r \approx 26$, thus indicating negative fluid damping. Off-resonance, the variation of the ratios is consistent with the linear analysis of the fluid–cylinder system for relatively small

U_r. When $U_r > 15$, the ratios are quite comparable in the lift and drag directions, probably the result of a small fluid damping in the present case. The cross-flow fluid damping becomes significant at $T/d = 1.13$, accounting for about one half of the effective damping. The third-mode effective damping ratio $\zeta_{y,e}^{(3)}$ is appreciably smaller than that corresponding to the first or second mode. This could be attributed to a substantial decrease of the structural damping ratios for higher modes of vibrations, as suggested by the linear analysis of the fluid–cylinder system.

The authors wish to acknowledge support given to them by the Central Research Grant of The Hong Kong Polytechnic University through Grant G-V529 and the Research Grants Council of the Government of the HKSAR through Grants PolyU5125/98E, and PolyU5128/98E.

REFERENCES

Bearman, P. W. & Wadcock, A. J. 1973 The interference between a pair of circular cylinders normal to a stream. *J. Fluid Mech.* **61**, 499–511.

Biermann, D. & Herrnstein, W. H., Jr 1933 The interference between struts in various combinations. *National Advisory Committee for Aeronautics, Tech. Rep.* 468.

Blevins, R. D. 1975 Vibration of a loosely held tube. *J. Engng Indust.* **97**, 1301–1304.

Blevins, R. D. 1994 *Flow-Induced Vibration.* Krieger.

Bloor, M. S. 1964 The transition to turbulence in the wake of a circular cylinder. *J. Fluid Mech.* **19**, 290–304.

Cantwell, B. & Coles, D. 1983 An experimental study of entrainment and transport in the turbulent near wake of a circular cylinder. *J. Fluid Mech.* **136**, 321–374.

Chen, S. S. 1987 *Flow-Induced Vibration of Circular Cylindrical Structures*, pp. 52–55. Hemisphere.

Evangelinos, C. & Karniadakis, G. E. 1999 Dynamics and flow structures in the turbulent wake of rigid and flexible cylinders subject to vortex-induced vibrations. *J. Fluid Mech.* **400**, 91–124.

Gerrard, J. H. 1966 The mechanics of the formation region of vortices behind bluff bodies. *J. Fluid Mech.* **25**, 401–413.

Granger, S., Campistron, R. & Lebret, J. 1993 Motion-dependent excitation mechanisms in a square in-line tube bundle subject to water cross-flow: an experimental modal analysis. *J. Fluids Struct.* **7**, 521–550.

Ishigai, S., Nishikawa, E., Nishmura, K. & Cho, K. 1972 Experimental study on structure of gas flow in tube banks with tube axes normal to flow (Part 1, Karman vortex flow around two tubes at various spacings. *Bull. JSME* **15**, 949–956.

James, M. L., Smith, G. M., Wolford, J. C. & Whaley, P. W. 1994 *Vibration of Mechanical and Structural Systems with Microcomputer Applications*, pp. 57–61. Harper Collins College Publishers.

Jin, W., Zhou, Y., Chan, P. K. C. & Xu, H. G. 2000 An optical fibre Bragg grating sensor for flow-induced structural vibration measurement. *Sensors and Actuators* **79**, 36–45.

Kamemoto, K. 1976 Formation and interaction of two parallel vortex streets. *Bull. JSME* **19**, 283–290.

Kim, H. J. & Durbin, P. A. 1988 Investigation of the flow between a pair of circular cylinders in the flopping regime. *J. Fluid Mech.* **196**, 431–448.

Kiya, M., Arie, M., Tamura, H. & Mori, H. 1980 Vortex shedding from two circular cylinders in staggered arrangement. *Trans. ASME: J. Fluids Engng* **102**, 166–173.

Landweber, L. 1942 Flow about a pair of adjacent, parallel cylinders normal to a stream. *D. W. Taylor Model Basin, Rep. 485.* Department of the Navy, Washington, DC.

Mignolet, M. P. & Red-Horse, J. R. 1994 ARMAX identification of vibrating structures: model and model order estimation. In *Proc. 35th Structures, Structural Dynamics, and Material Conference, AIAA/ASME, Hilton Head, South Carolina, April 18–20*, pp. 1628–1637.

Nayfeh, A. H. & Mook, D. T. 1995 *Nonlinear Oscillations*, pp. 96–97. John Wiley & Sons.

Prandtl, L. 1935 The mechanics of viscous fluid. Reprinted in *Aerodynamics Theory: A General Review of Progress* (ed. W. F. Durand). Gloucester Mass., Peter Smith Publisher, 1976.

Price, S. J. & Paidoussis, M. P. 1989 The flow-induced response of a single flexible cylinder in an in-line array of rigid cylinders. *J. Fluids Struct*. **3**, 61–82.

Qaudflieg, H. 1977 Vortex induced load on the cylinder pair at high *Re. Forsch. Ing. Wes.* **43**, 9–18.

Rao J. S. 1992 *Advanced Theory of Vibration*, pp. 132–134. John Wiley & Sons.

So, R. M. C., Liu, Y., Chan, S. T. & Lam, K. 2001 Numerical studies of a freely vibrating cylinder in a cross flow. *J. Fluid Struct*. (to appear).

So, R. M. C., Zhou, Y. & Liu, M. H. 2000 Free vibrations of an elastic cylinder in a cross flow and their effects on the near wake. *Exps. Fluids* **29**, 130–144.

Spivac, H. M. 1946 Vortex frequency and flow pattern in the wake of two parallel cylinders at varied spacings normal to an air stream. *J. Aero. Sci.* **13**, 289–297.

Sumner, D., Wong, S. S. T., Price, S. J. & Paidoussis, M. P. 1999 Fluid Behaviour of side-by-side circular cylinders in steady cross-flow. *J. Fluids Struct*. **13**, 309–338.

Wang, X. Q:, So, R. M. C. & Liu, Y. 2000 Flow-induced vibration of an Euler-Bernoulli beam. *J. Sound Vib*. **243**, 241–268.

Weaver, D. S. & Abd-Rabbo, A. 1984 A flow visualization study of a square array of tubes in water cross-flow. *Proc. Symp. On Flow-Induced Vibrations*, Vol. 2 (ed. M. P. Paidoussis, M. K. Au-Yang & S. S. Chen), pp. 165–177.

Weaver, W., Timoshenko, S. P. & Young, D. H. 1989 *Vibration Problems in Engineering*, 5th edn, pp. 54–55, 366, 426–432 & 454–456. John Wiley & Sons.

Williamson, C. H. K. 1985 Evolution of a single wake behind a pair of bluff bodies. *J. Fluid Mech.* **159**, 1–18.

Zdravkovich, M. M. 1977 Review of flow interference between two circular cylinders in various arrangements. *Trans. ASME: J. Fluids Engng* **99**, 618–633.

Zdravkovich, M. M. 1985 Flow-induced oscillations of two interfering circular cylinders. *J. Sound Vib*. **101**, 511–521.

Zdravkovich, M. M. 1987 The effects of interference between circular cylinders in cross flow. *J. Fluids Struct*. **1**, 239–261.

Zdravkovich, M. M. & Pridden, D. L. 1977 Interference between two circular cylinders; series of unexpected discontinuities. *J. Indust. Aerodyn.* **2**, 255–260.

Zhou, Y. & Antonia, R. A. 1994 Effect of initial conditions on structures in a turbulent near-wake. *AIAA J*. **32**, 1207–1213.

Zhou, Y., SO, R. M. C., Jin, W., Xu, H. G. & Chan, P. K. C. 1999 Dynamic strain measurements of a circular cylinder in a cross flow using a fibre Bragg grating sensor. *Exps. Fluids* **27**, 359–367.

Zhou, Y., So, R. M. C., Liu, M. H. & Zhang, H. J. 2000*a* Complex turbulent wakes generated by two and three side-by-side cylinders. *Intl J. Heat Fluid Flow* **21**, 125–133.

Zhou, C. Y., So, R. M. C. & Mignolet, M. P. 2000*b* Fluid damping of an elastic cylinder in a cross flow. *J. Fluids Struct*. **14**, 303–322.

Ziada, S. & Staubli, T. (eds.) 2000 *Flow-Induced Vibration*. A. A. Balkema.